Activatable photoacoustic lifetime probe for imaging of enzyme activity

A Dissertation
SUBMITTED TO THE FACULTY OF
UNIVERSITY OF MINNESOTA
BY

Ekaterina Morgounova Ippolito

IN PARTIAL FULFILLMENT OF THE REQUIREMENTS
FOR THE DEGREE OF
DOCTOR OF PHILOSOPHY

Adviser: Dr. Shai Ashkenazi

April 2017

Acknowledgements

Firstly, I would like to express my sincere gratitude to my advisor, Prof. Shai Ashkenazi, for his continuous support during my PhD, for his guidance, his encouragements, his patience, and his genuine kindness, which were all critical for my professional development and the success of my project. I consider myself lucky to have been mentored by someone with such depth of technical knowledge and such a caring nature. For this, I am forever grateful, and I know I will remember my PhD years fondly. I also would like to thank Rina, his wife, for creating a sense of family during lab gatherings. The completion of this dissertation marks the end of my work in the lab, but not the end of our friendship which I hope will last for many years to come.

Besides my advisor, I am also very grateful to my academic collaborators and dissertation committee members, Prof. Benjamin J. Hackel and Prof. Michael Wilson, for their insightful comments which drove me to consider my research from an inter-disciplinary perspective, for motivating me to develop and foster my technical, analytical and writing skills, and above all for their presence in my life as warm and generous mentors. I also would like to thank Prof. Paolo Provenzano for his support during my PhD, for serving in my committee, and for reviewing my dissertation; as well as Prof. David D. Thomas for his astute guidance early on in my project.

I would like to express my heartfelt gratitude to my close collaborator Sadie M. Johnson, for her relentless dedication, hard work and enthusiasm which made the completion of this project possible (our working and moral support sessions at the nearby coffee shop truly made the difference).

I also would like to give special thanks to my lab brothers and sisters: Clay Sheaff, for his technical mentoring and our brainstorming sessions, and for lending me an ear to voice my self-doubt and boosting my confidence; Amin M. Tadayon, for teaching me research management skills, and for being a role model of scientific and professional

maturity for me to emulate; and Supriya V. Thathachary, for being the kindest and most trusted confidante for personal and professional hurdles. I am incredibly lucky to have spent my PhD years with such supportive, kind-hearted and open-minded people that have become my lifelong friends. I also thank Qi, for a productive collaboration and for providing feedback that helped me improve my work.

I am very grateful to those who mentored or helped me in different capacities during my PhD: Meri DuRand, Paul Hsieh, and Jesse McCaffrey, among others; and to those I have mentored, especially my undergraduate students Sina Kassaw and Ashtynn Trauth, and Master's students Ankit Chadha and Saurabh Kotian.

I would like to extend my gratitude to all my academic friends who provided input and cheered for me during my PhD: Simeng (David) Zhang, June Baik, Alessandro Magli, Cynthia Hornbeck, Pantea Moghimi, Zaw Win, Viann Nguyen, Xiao Zhong, Yi-Jou (Tina) Yeh and Kanchan Kulkarni.

I am extremely grateful to my family for their unconditional love and emotional support throughout my life. My mother and grandmother are the strongest and most resilient people I know, yet they raised me with and to value kindness and compassion. I am also grateful to my parents-in-law who welcomed me into their home with open arms and shared my hopes and joys as if they were their own.

Last but not least, I would like to thank my husband, Joseph, the love of my life and my first cheerleader, for being a daily source of strength, motivation and happiness. I am lucky to have such an incredible, passionate, funny and sensitive partner to grow and go on life's adventures with. He inspires me every day with his accomplishments, and I know I am as proud of him as he is of me. May we be kind to each other, always.

Thank you. Merci. Grazie. Спасибо. תודה. متشكرم. நன்றி. 고맙습니다. 谢谢.

Dedication

This thesis is dedicated to my mother, Svetlana, and my husband, Joseph, who always supported and loved me, and to the memory of my beloved grandmother, Galina Ivanova.

Cette thèse est dédiée à ma mère, Svetlana, et à mon mari, Joseph, qui m'ont toujours soutenu et aimé, et à la mémoire de ma grand-mère chérie, Galina Ivanova.

Abstract

Photoacoustic molecular imaging (PMI) is a non-ionizing imaging modality that can provide functional and metabolic information at clinically relevant penetration depth (~ 2 cm) with submillimeter spatial resolution. This doctoral dissertation focuses on applying PMI to measure the activity of matrix metalloproteinase 2 (MMP-2), an enzymatic marker of cancer progression capable of altering the tumor microenvironment. Photoacoustic lifetime imaging (PALI) is used to probe the transient absorption of an activatable probe capable of changing its excited-state lifetime from short (1 – 10 ns) to long (1 – 10 μs) upon cleavage by MMP-2. Several models were developed to test the hypothesis of lifetime contrast between the inactive and active form of the probe. A series of peptide-based activatable photoacoustic probes of varying length and structure were synthesized. In order to enlighten the structure/function relationship and identify the optimal probe, we compared their dimerization and separation efficiency, activation rate, and photoacoustic lifetime signal strength with respect to a non-activatable control. Our long-term goal is to implement this technique to image the activity of enzymes involved in pathological processes in clinical settings. To this end, we have developed a portable multimodal imaging system for the simultaneous visualization of ultrasound anatomical images and PALI enzymatic activity. Ultimately, this technique could be translated into an early-stage cancer diagnostic or prognostic tool, as well as for personalized treatment planning or continuous monitoring of treatment efficacy.

Table of Contents

List of Tables

List of Figures

Preface

This thesis describes the step-by-step development of the first activatable photoacoustic imaging probe for enzyme activity detection based on lifetime contrast. It comprises materials that have been published or soon-to-be submitted for publication to academic journals and includes contributions by multiple authors.

Chapter 1: Introduction presents the clinical significance of this work for cancer diagnosis and treatment and the principles behind photoacoustic lifetime imaging. An example of photoacoustic lifetime imaging applied to tumor hypoxia mapping was adapted from *In vivo photoacoustic lifetime imaging of tumor hypoxia in small animals* by Q. Shao, E. Morgounova (Ippolito), C. Jiang, J. Choi, J. Bischof, and S. Ashkenazi in the Journal of Biomedical Optics 18(7) (2013) [53]. In this example, the animal work and data analysis were performed by Q. Shao. E. Ippolito provided support and input with experiment conception and manuscript revision.

Chapter 2: A chemical model for MB dimerization describes the testing of the hypothesis of lifetime switching from high (1-10 μs) to low (1-10 ns) between methylene blue monomers and dimers. This work was published in *Photoacoustic lifetime contrast between methylene blue monomers and self-quenched dimers as a model for dual-labeled activatable probes* by E. Morgounova (Ippolito), Q. Shao, B. J. Hackel, D. D. Thomas, and S. Ashkenazi in the Journal of biomedical optics 18(5) (2013) [115]. Experiment conception and implementation, data analysis and manuscript writing were performed by E. Ippolito. S. Ashkenazi oversaw the project. Q. Shao, D. D. Thomas, and S. Ashkenazi provided input with experiment conception and reviewed the manuscript.

Chapter 3: Activatable probe design and evaluation presents the design, synthesis and evaluation of a series of activatable photoacoustic probe. This work is under review and will soon be submitted for publication as: *Engineering a Lifetime-Based Activatable Photoacoustic Probe for Matrix Metalloproteinase 2* by E. M. Ippolito, S. M. Johnson, B. J. Hackel, M. Wilson, and S. Ashkenazi. It is partly adapted from *Lifetime-based photoacoustic probe activation modeled by a dual methylene blue-lysine conjugate,* Proceedings of SPIE, 89435F (2014), and *In vitro characterization of a lifetime-based activatable photoacoustic probe,* Proceedings of SPIE, 93232J (2015), by the same authors. E. Ippolito conceived, performed and analyzed photoacoustic experiments, and conceived and analyzed absorption and kinetics experiments. S. Johnson performed conjugation and peptide synthesis, and conceived and performed kinetic experiments. Both E. Ippolito and S. Johnson performed absorption experiments. B. J. Hackel, M. Wilson, and S. Ashkenazi oversaw the project. E. Ippolito wrote the manuscript with support and input from all the authors.

Chapter 4: Towards in vivo imaging presents unpublished work by E. Ippolito on the development of a multimodal system for combined US/PA/PALI imaging. S. Ashkenazi oversaw the project.

Chapter 1.

Introduction

1.1 CLINICAL SIGNIFICANCE

1.1.1 *Cancer incidence and approach to treatment*

Current estimates indicate that one of three Americans are or will be affected by cancer during their lifetime, and that the incidence of cancer rate has doubled in the past 20 years [1]. Cancer is caused by an accumulation of genetic mutations affecting cellular regulatory pathways such as pro-angiogenic growth factors, tumor suppressor genes, and apoptotic regulators, among others [2]. The incidence of cancer has been correlated with both genetic and environmental factors – including family history, lifestyle, and exposure to carcinogenic agents [3]. Due to the genetic complexity and variability across different cancer types, it is nearly impossible to eliminate all cancers, nor is it currently possible to reprogram cancer cells to revert to their normal state [4]. For now, the one key to reduce cancer incidence and cancer-associated deaths consists in early, accurate diagnosis at a pre-cancerous or treatable stage. In addition, personalized medicine, or the use of individual genomic, proteomic (e.g. enzymes) and metabolic (e.g. oxygen) information to guide treatment options, can improve tumor response and survival rates [5]. Finally, combining tumor localization and molecular characterization into a single step can deliver a powerful tool for early diagnosis and treatment monitoring.

1.1.2 *Current and emerging methods for cancer diagnosis*

A first class of cancer diagnosis tools are screening tests that rely on blood samples, such as prostate-specific antigen (PSA) [6], or stool samples, such as multi-target stool DNA [7], to detect the presence of cancer biomarkers. In general, these tests have limited accuracy and require a confirmation of diagnosis using more invasive techniques.

Several noninvasive imaging modalities are commonly used for the detection of tumor masses, such as computed tomography (CT), positron tomography (PET), magnetic resonance imaging (MRI), and ultrasound imaging (US) [8], sometimes in combination with contrast agents. Each technique possesses a spatial resolution/imaging depth trade-off (Figure 1.1) which defines their applicability to different types of tumor. They also present individual limitations in clinical settings, such as ionizing radiations for nuclear imaging, low sensitivity and high cost for MRI, and low organ/tumor contrast for ultrasound.

Biopsy is currently the preferred method to confirm cancer diagnosis, as it provides information about histological type, classification, grade, and aggressiveness which may help determine the best treatment [9]. In some cases, especially for tumors located in deep-seated organs like the prostate or the liver, ultrasound imaging may be used to guide the biopsy needle towards the tumor site. In other cases, such as polyp resection in the colon or the lungs, an endoscopic camera guides biopsy snare or forceps to the suspected area. Biopsy is always an invasive and painful procedure that may cause injury and spread of the disease [10]. Possible complications include spread of tumor cells, fever, infection, and

bleeding. Finally, very small tumors (< 1 mm) may be missed by ultrasounds or the biopsy needle may not be able to accurately target them or to obtain a decent sample size.

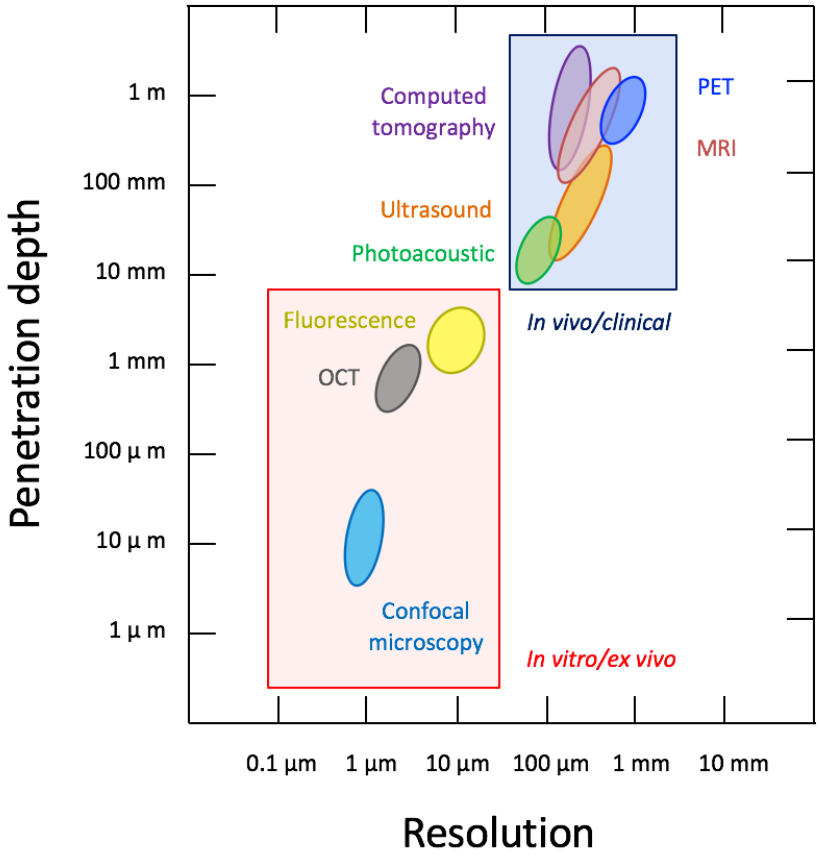

Figure 1.1. Comparative trade-off between resolution and penetration depth for different imaging modalities. Abbreviations: MRI, magnetic resonance imaging; PET: positron emission tomography; OCT, optical coherence tomography.

More recently, molecular imaging techniques have sought to simultaneously localize and characterize tumors non-invasively. By providing a map of metabolic or molecular expression or activity, they may help differentiate between a benign and a cancerous tumor, or between cancer and other pathologies (e.g. stomach cancer versus ulcer), therefore reducing the risk of unnecessary biopsies. Several molecular probes for

clinically relevant modalities have been tested in animals and in humans, including targeted microbubbles for ultrasound [11], targeted magnetic nanoparticles for MRI [12] and radiolabeled probes for PET [13]. For cancer research, the most widely used technique is fluorescence imaging of near-infrared (NIR) probes [14-20]. Fluorescent probes can yield a highly specific contrast signal, but their imaging depth is limited to a few millimeters due to the diffuse nature of photon propagation in tissue, and their resolution deteriorates exponentially with increasing depth (Figure 1.1) [21]. Finally, photoacoustic (PAI) imaging, which combines the high contrast of optical molecular probes with the relatively high imaging depth and resolution of ultrasound, has been gaining grounds in preclinical studies and is recently being evaluated for breast cancer diagnosis [22].

1.1.1 *Proteolytic markers for cancer diagnosis and treatment*

Proteases are enzymes that catalyze the hydrolytic cleavage of peptide bonds and participate in a variety of critical biological processes. In particular, proteases enable cancer cells to adapt to the topology of the primary and secondary tumor sites by altering the microenvironment [23]. Tumor-promoting proteases function as part of an extensive proteolytic network which interacts with cancer signaling pathways, simultaneously controlling and amplifying proteolytic activity during cancer progression [24, 25].

Matrix metalloproteinases (MMPs) are a family of proteases that degrade proteins in tissue extracellular matrices (ECM) [26]. Such effects occur during embryogenesis and normal physiological tissue remodeling such as wound healing, but also during pathological processes such as tumor angiogenesis, invasion and metastasis [27-29], and

in inflammation related disease [30-32], arthritis [33, 34], and artherosclerosis [35, 36]. Their mode of action during cancer progression include promoting angiogenesis by recruiting vascular-associated pericytes, degrading ECM collagen to facilitate cell migration in the stroma, and degrading the basement membrane which allows cells to intravasate into the blood vessels [37]. MMPs inhibitors have been extensively studied as drug targets for cancer therapy [38], but those treatments have met with limited success so far, possibly due to the complexity of their signaling activities.

Many different MMPs are typically overexpressed at any given point during tumorigenesis, however the overexpression of individual MMPs is differently regulated in time and among cell types [39]. In particular, type IV collagenases (MMP-2 and MMP-9) levels have been consistently reported by several studies to be up-regulated in biopsies and tissue specimens of prostate cancer [28, 39, 40]. We chose MMP-2 as our first target because it is among the best characterized proteases overexpressed by tumors.

Developing a molecular probe that enable imaging of protease activity in living subjects with high resolution will have a contribution in the following areas: 1) basic research: to study the role of proteases in disease initiation and progression in animal models and to improve our understanding of underlying biological processes in cancer progression, 2) drug development: to visualize and quantify protease activity for the development of enzyme-mediated and enzyme-suppression drugs for cancer and other conditions caused by uncontrolled extra-cellular degradation, 3) clinical practice: to diagnose high expression levels for proteases and to monitor treatment efficacy in prostate cancer patients.

1.2. PHOTOACOUSTIC IMAGING TECHNIQUES AND APPLICATIONS

1.2.1 *Photoacoustic Imaging (PAI)*

PAI can surpass the imaging depth and resolution limitations of fluorescence imaging while simultaneously keeping the high contrast provided by the absorption differential between optical contrast agents and tissues [41]. It consists of laser pulse excitation followed by the detection of ultrasound waves generated by the thermoelastic expansion of absorbing molecules (Figure 1.2). Because the scattering of ultrasound waves is much weaker than that of light, the signal can propagate back from the generation site through several centimeters without significant attenuation. Backpropagation algorithms like those employed for ultrasound reconstruction are then used to reconstruct an image which is related to the optical energy distribution in the sample.

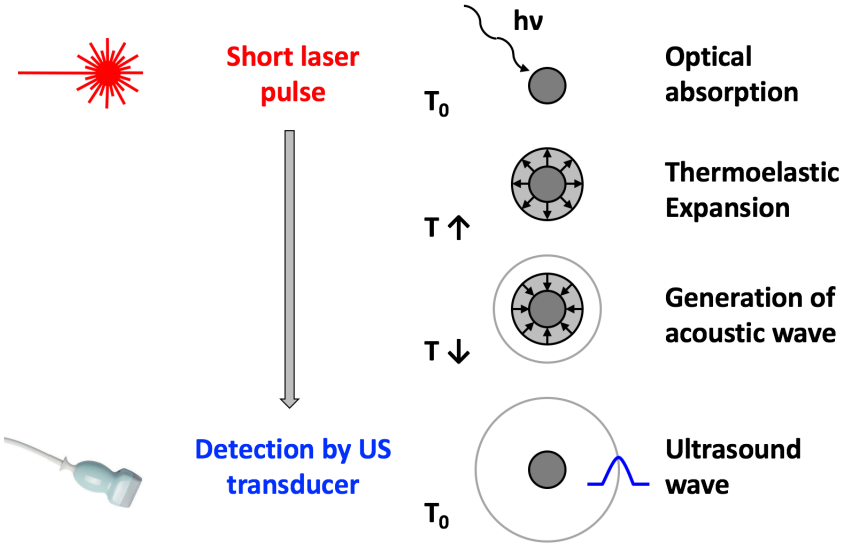

Figure 1.2. Explanation of the photoacoustic effect.

The implementation of PAI in biomedical applications has rapidly evolved during the last decade. Imaging penetration depth of up to 5 cm has been demonstrated [42]. The resolution is determined by the bandwidth of the ultrasound transducer and is similar to that ultrasound pulse/echo imaging (0.2 to 0.02 mm) [43]. Contrast agents for PAI can be either endogenous – such as blood, lipids and melanin – or exogenous – such as dyes [44], metallic nanoparticles [45], carbon nanotubes [46] and even quantum dots [47]. PAI have been demonstrated in applications such as: imaging of blood vasculature [48], cancer tumor angiogenesis detection [49], lymph nodes imaging [49], and skin cancer imaging [50].

1.2.2 *Photoacoustic pump-probe approach for excited-state lifetime probing*

In laser physics, the pump-probe technique has been used to probe the transient excited state of photoabsorbing molecules. An example of molecules with a long excited-state lifetime are oxygen-sensitive dyes such as Methylene Blue (MB). MB has an absorption peak in the UV region (300 nm) and an even stronger peak in the NIR window (660 nm) where tissue absorption is minimal (Figure 1.3). When excited by a laser source, MB molecules transition from the ground state (S_0) to a singlet excited state (S_1) in a few femtoseconds, then spontaneously undergo intersystem-crossing (ISC) to a metastable triplet state (T_1) (Figure 1.4). The triplet excited-state lifetime of MB was measured at 79.5 μs in degassed water, but drops dramatically to 1.8 μs in air-saturated solution due to collisional, or dynamic, quenching with oxygen [51].

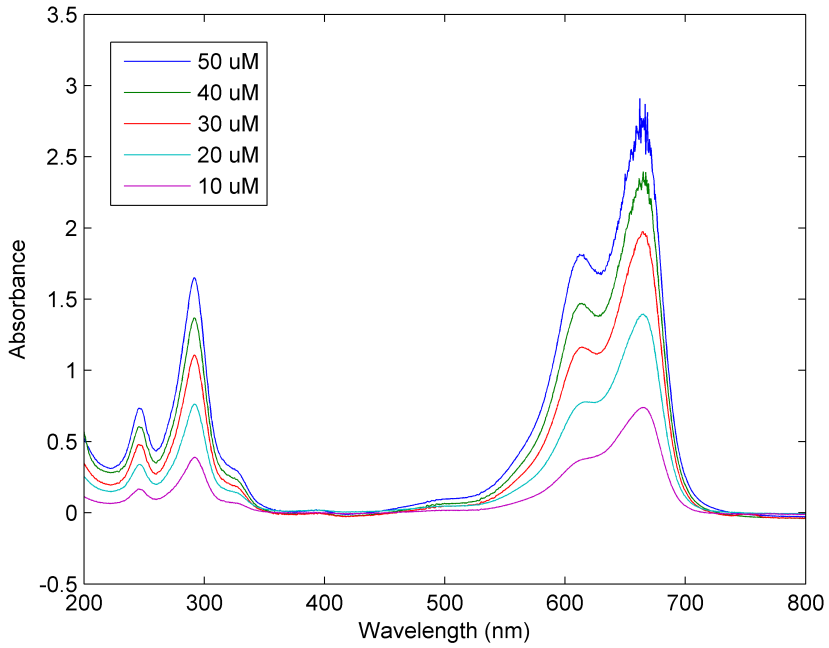

Figure 1.3. Absorption spectra of MB chromophore for different concentrations.

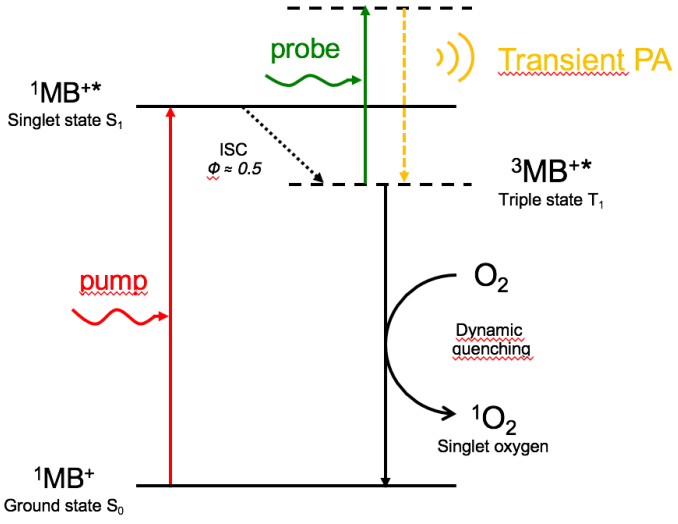

Figure 1.4. Energy diagram of MB chromophore.

Photoacoustic pump-probe measurement of the excited-state lifetime of MB happens in two steps. First, a laser pulse pumps MB to its excited state, then a second laser pulse is fired after the pump pulse to probe the triplet excited state by generating PA waves (Figure 1.5(a)). By repeating a sequence of pump-probe pulses with increasing time delays, it is possible to extract the excited-state lifetime by exponential fitting of the photoacoustic amplitude signal at each measurement point (Figure 1.6). Finally, the pump and probe laser wavelengths are chosen to produce the maximum of photoacoustic emission at 660 nm and 840 nm, respectively (Figure 1.5(b-c)).

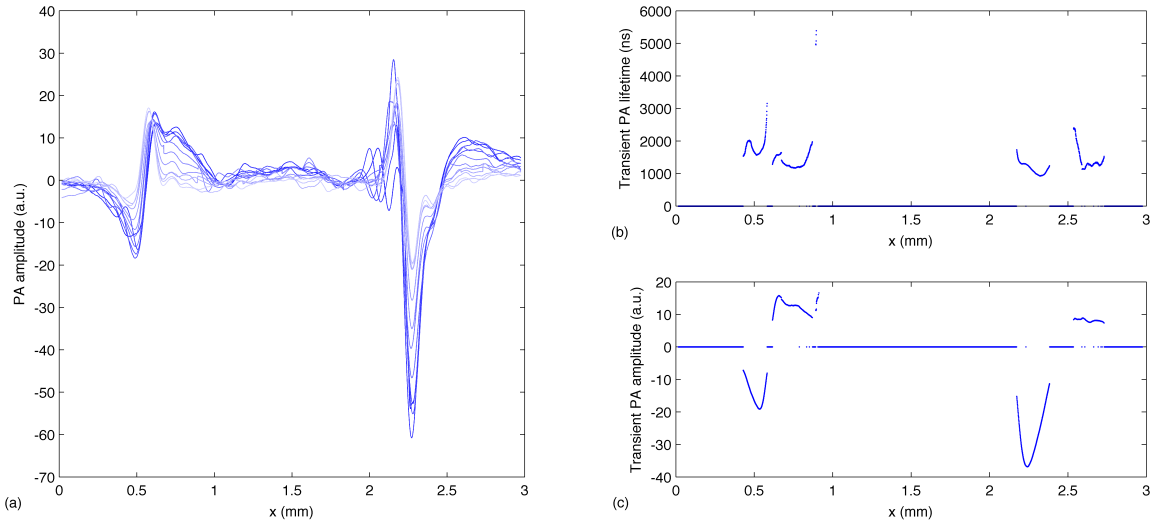

Figure 1.6. (a) Photoacoustic amplitude signal of a plastic tube filled with MB dye at different pump-probe delay times. The two waveforms correspond to the back (x = 0.6 mm) and front (x = 2.2 mm) dye-plastic interfaces. (b) Photoacoustic excited-state lifetime as a function of position. The lifetime τ was calculated by applying an exponential fit to the PA amplitude data (PA = tPA*exp(-t/τ) + DC). Data points for which $R^2 <$ 0.95 were excluded from the graph. (c) Transient photoacoustic amplitude (tPA) as a function of position.

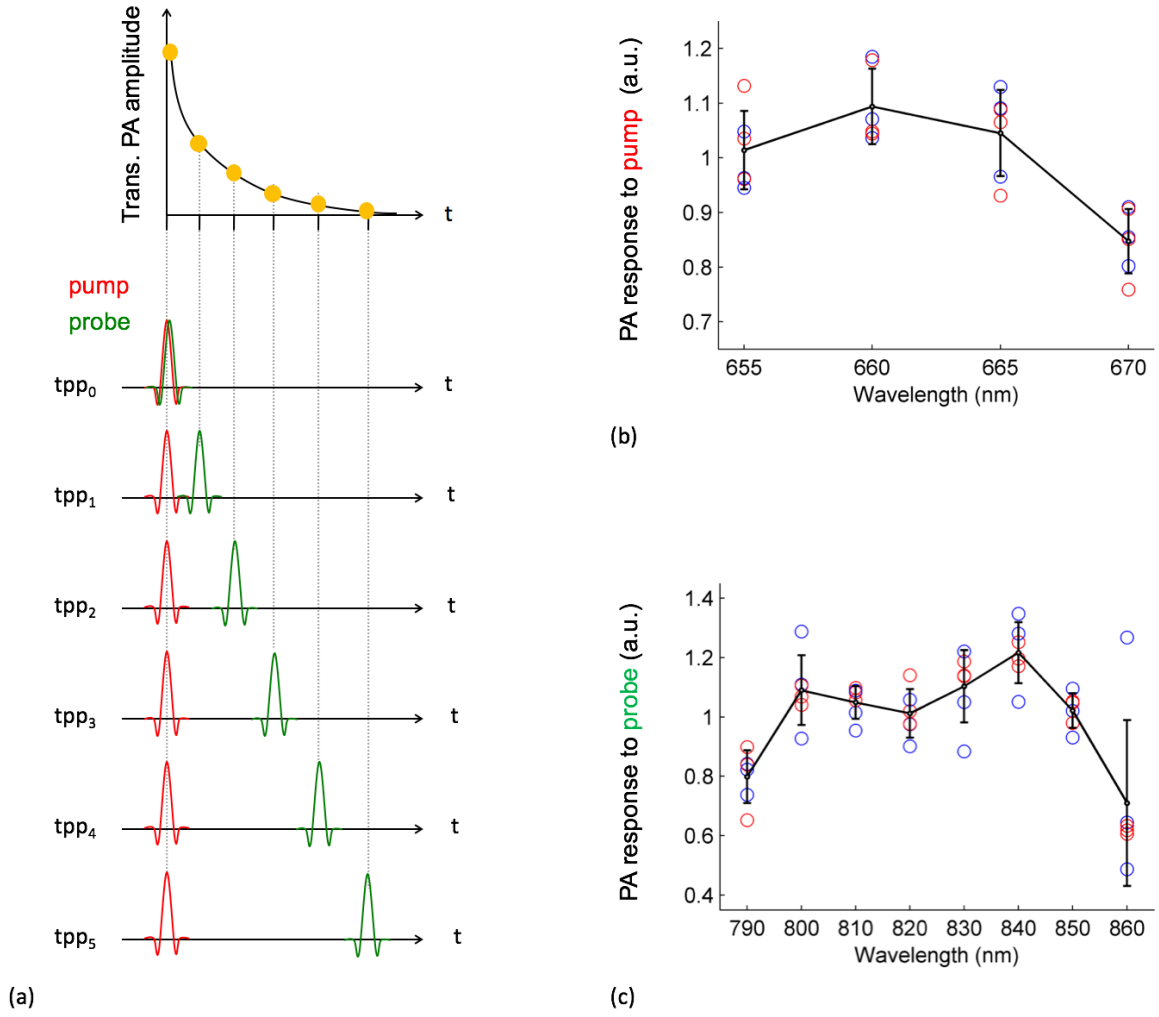

Figure 1.5. (a) Pump-probe approach for photoacoustic imaging. *tpp*: pump-probe delay. (b) Photoacoustic response of MB chromophore for different pump wavelengths. (c) Transient photoacoustic response of MB chromophore for different probing wavelengths.

1.2.3 *Photoacoustic Lifetime Imaging (PALI) for oxygen mapping*

PALI implements the photoacoustic pump-probe approach to yield 2D images of the oxygen level in tissue. Excited-state lifetime (τ) and oxygen partial pressure (pO_2) are related by the Stern-Volmer relationship:

$$\frac{\tau_0}{\tau} = 1 + k_Q \tau_0 pO_2$$

Where τ_0 = 79.5 μs, the lifetime at pO_2 = 0 mmHg, and k_Q = 0.0036 $\mu s^{-1}.mmHg^{-1}$, the quenching rate constant [51].

Our group has recently reported on the *in vivo* imaging of tumor hypoxia using PALI [52]. Tumors were induced in nude mice by subcutaneous injection of LNCaP cells into their hindlimbs. The tumors were grown for 3 - 5 weeks until they reached a diameter of 5 - 10 mm. The animals were then anesthetized and injected intratumorally with MB dissolved in physiological saline solution. The dye was left to diffuse for 10-15 minutes and the animals were then imaged inside a heated water bath (35°C). Ultrasound images were acquired to provide the anatomical structure of the hindlimb, and reconstructed using the synthetic transmit aperture (STA) method [53] (Figure 1.7(a)). PA images were then acquired for increasing pump-probe delay times, averaged over a hundred measurement to compensate for laser energy variations, and reconstructed using a backprojection algorithm (Figure 1.7(c)). The total PA image acquisition lasted approximately 150 seconds. Finally, the PALI image was reconstructed by first subtracting the background tissue signal (Figure 1.7(b)) from the PA images and then calculating the lifetime for each pixel (Figure 1.7(d)). A hypoxic region was found at the site of the tumor, whereas normal tissue showed an oxygenation within the normal physiological range (Figure 1.7(e)).

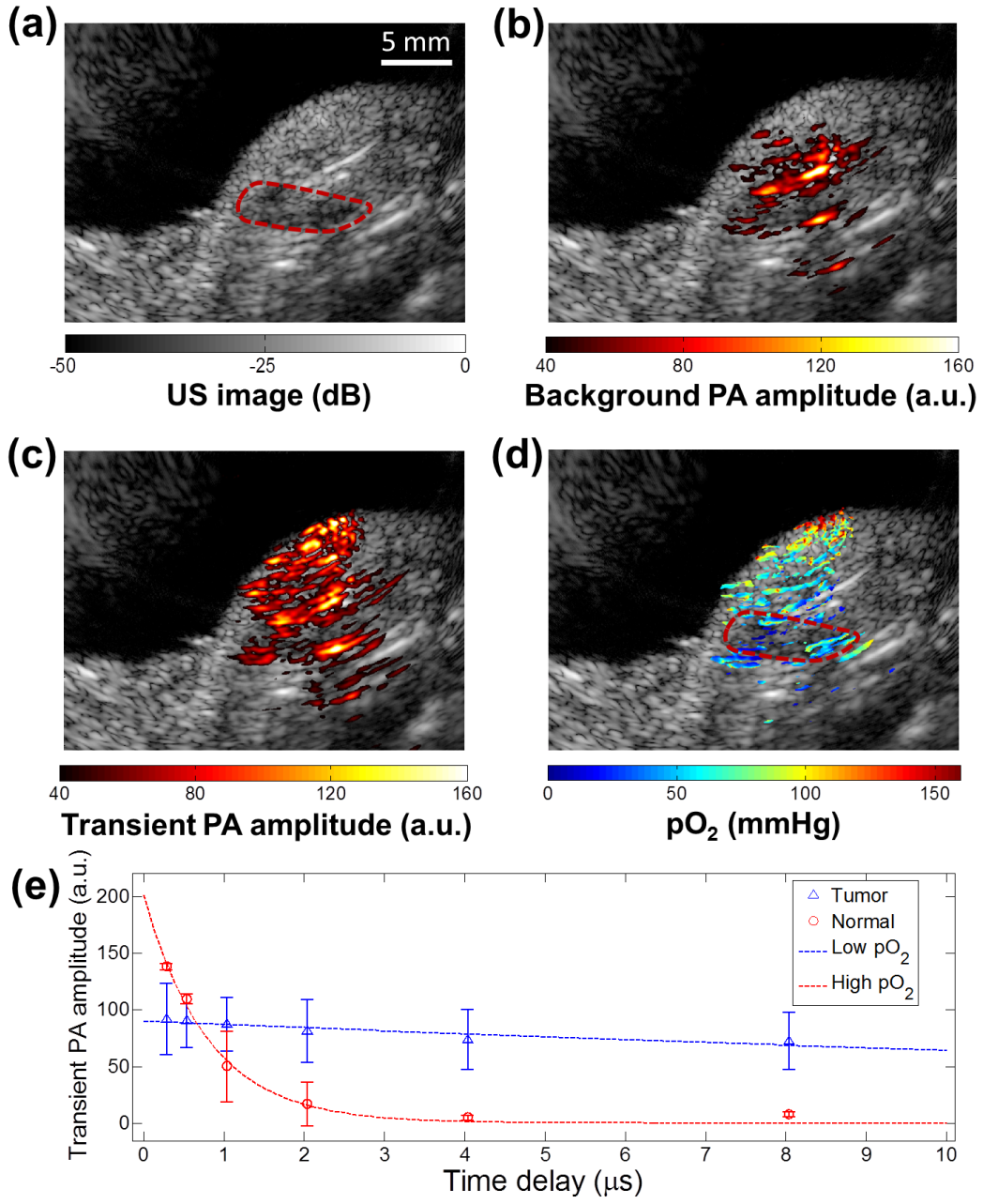

Figure 1.7. (a) Ultrasound image of the left tumor-bearing hindlimb of a mouse. The area of the tumor is enclosed by a red dashed line. (b) Background tissue absorption at 810 nm. (c) Transient PA amplitude at a pump-probe delay of 0.25 μs. (d) pO2 map obtained from PALI (e) Transient PA amplitude of two representative pixels within the tumor and in normal control tissue. The error bars represent the standard deviation over 100 recordings. The dashed lines represent the exponential fitting curve.[1]

[1] Animal work and data analysis were performed by Q. Shao [52]

1.2.4 *Current activatable probes for photoacoustic imaging*

The advantages of PA imaging have led to the recent development of several photoacoustic activatable probes to image the activity of proteolytic enzymes [54-56]. These probes are comprised of a fluorophore-quencher pair held together by a peptide linker or structure with one or more activation sites. Nearly invisible in their inactive state, they can be switched on upon interaction with a target enzyme.

Regression analysis is used to measure differences in photoacoustic absorption arising from probe activation. Ideally, the number of wavelengths used to resolve changes in the absorption spectra should be at least equal to the number of independent components in tissues (inactive and active probe, hemoglobin, deoxyhemoglobin, etc…). The underlining assumption is that the PA signal is a linear function of the absorption spectrum of the tissue components. This assumption, however, only holds in an approximate way at shallow depths. As light penetrates deeper into the tissue, its spectral distribution changes due to the absorption by endogenous chromophores. It also changes due to scattering which is wavelength dependent. Thus, the spectral shape of the illumination at a fixed point in the tissue is not known, and therefore the PA signal generated at this point does not reflect the true absorption spectrum. The situation is akin to having an optical spectrometer without the option of taking a reference spectrum for compensating the spectral shape of the lamp. This inherent non-linearity of multi-spectral PAI is well known and has been addressed by several groups [57, 58]. This effect limits imaging of activatable probes by PA imaging due to the difficulty in suppressing tissue background and non-activated probe signal.

1.2.5 *Activatable photoacoustic lifetime probe*

For my dissertation, I developed a more robust activatable probe design based on the lifetime contrast between the inactive and active form of the probe. Efficient intersystem crossing to the metastable triplet state in MB monomers results in long excitation lifetime. MB dimers, on the other hand, have a very short lifetime due to static quenching. Furthermore, in addition to absorbing weakly at the wavelengths used to excite and probe excited-state MB, the lifetime of relevant tissue components is at least three orders of magnitude shorter than that of MB monomers (Table 1.1). These properties can be exploited to design a dually-labeled activatable probe which produces extremely high contrast. The distinct separation of time-scales allows for efficient suppression of all PA signals arising from absorbers having lifetimes shorter than a set threshold.

Molecule	**Lifetime (ns)**
Myoglobin	0.1 [59]
Melanin	0.14 [60]
Albumin	4.8 [61]
Deoxyhemoglobin	0.2 [62]
Oxyhemoglobin	0.22 [62]
MB dimers/inactive probe	40 [63]
MB monomers/active probe	> 1800 [51]

Table 1.1: Excited-state lifetime of activatable lifetime probe in its two states and main tissue components.

MB dimerization and lifetime are affected by changes in pH and temperature. Previous studies showed that the pH of tumors is significantly lower and exhibits more variability (from about 5.8 to about 7.6) than the pH of surrounding tissues (from 7.00 to 8.06) [64]. Absorption measurements of potassium phosphate buffered MB solutions (pH 5-8) revealed that pH levels in that range do not have a considerable effect on MB dimerization compared to the aggregative effect of sodium sulfate, a salt known to artificially increase MB dimerization and studied in Chapter 2 (Figure 1.8). Similarly, an increase in temperature has a disaggregating influence on the absorption spectrum of dimer dyes [65], but this effect is insignificant compared to that of salt-induced dimerization. Finally, it should be noted that at pH < 6 the excited-state lifetime was shown to decrease from 36 to 4 μs in nitrogen purged solution [66].

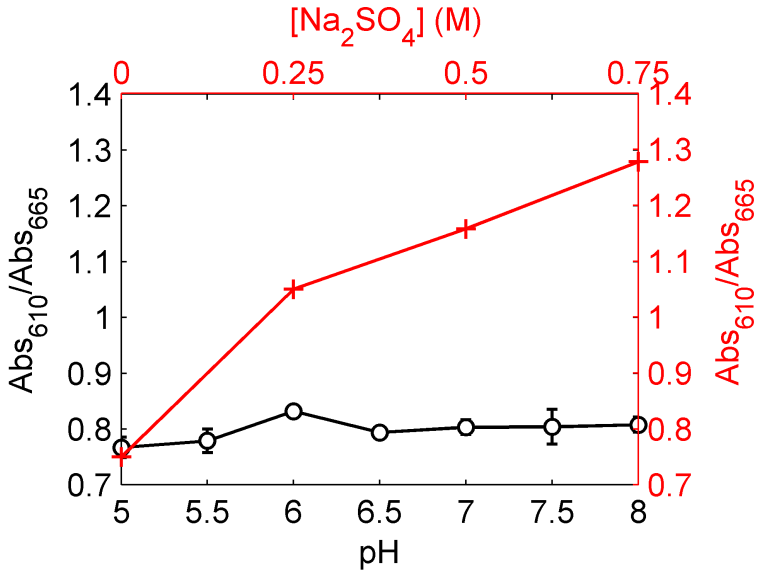

Figure 1.8. Dimer-to-monomer ratio of MB at different pH levels and different sodium sulfate (Na_2SO_4) concentrations. The error bars represent the standard deviation over 3 measurements.

Chapter 2. A chemical model for MB dimerization

Photoacoustic lifetime contrast between methylene blue monomers and self-quenched dimers as a model for dual-labeled activatable probes.

2.1 INTRODUCTION

Photoacoustic molecular imaging is a non-ionizing modality that provides high penetration depth and high spatial resolution information on the functional and metabolic status of diseases at greater depths than other optical imaging techniques [41, 55, 56]. Traditionally, photoacoustic imaging has been used with both endogenous (e.g. hemoglobin and melanin) and exogenous contrast agents that exhibit higher optical absorption than normal tissue. Targeting molecular markers using exogenous smart probes can potentially reap valuable information about biological processes occurring at different stages of various diseases. As a result, photoacoustic molecular imaging could substantially aid the diagnosis of cancer by detecting subtle abnormalities at the molecular level well before the appearance of anatomical changes [67]. This capability would also allow for personalized treatment planning and step-by-step evaluation of treatment efficacy [56].

Our research focuses on the development of a new photoacoustic contrast agent based on the lifetime sensing of methylene blue (MB) dye. MB monomers present a high quantum yield of intersystem crossing ($\Phi_{ISC} > 0.50$) [68] and a long triplet excited-state lifetime ($\tau > 70$ μs) [51]. Upon aggregation, static quenching between strongly bonded molecules dramatically shortens their excited-state lifetime by two to three orders of

magnitude [69]. This forms the basis of a highly-sensitive contrast mechanism between MB monomers and dimers. A promising application is the development of a MB-labeled smart probe activated by enzymatic cleavage. The probe's signal is highly suppressed in the bound state, but it recovers its long excited-state lifetime after activation, which is then detectable by photoacoustic lifetime contrast imaging (PLCI) (Figure 2.1).

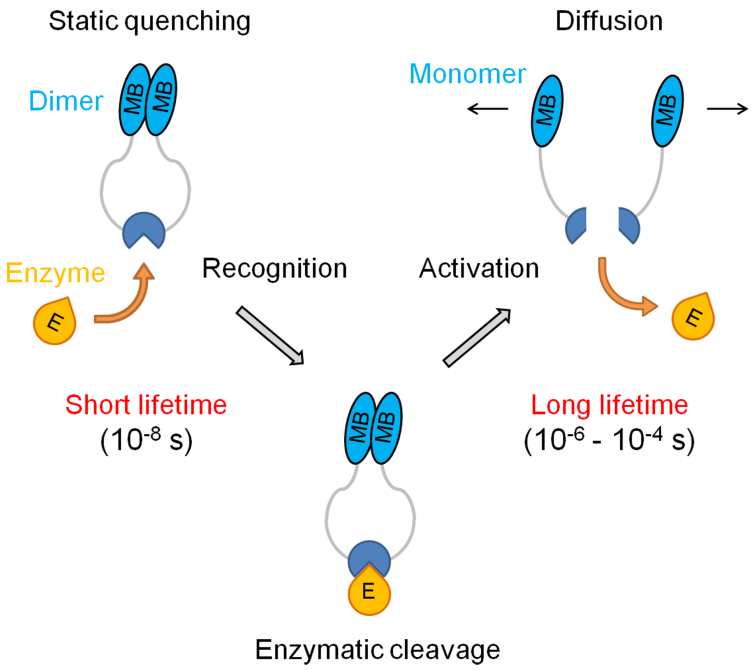

Figure 2.1. Schematic representation of proposed MB dual-labeled activatable probe containing a specific enzymatic site. The intact probe has a short lifetime of a few tens of nanoseconds. Enzymatic cleavage separates the chromophores thereby permitting them to recover their long excited-state lifetime (tens of microseconds).

2.1.1 *Activatable probes for molecular imaging*

Activatable probes are a class of contrast agents that identify selective enzyme activity by switching from an inactive state to an active state upon interaction with a target enzyme [20]. Originally developed for fluorescence imaging, the probes contained a fluorophore-quencher pair coupled to a peptide linker bearing an enzymatic site [70]. Upon cleavage of the linker, the pair is separated and fluorescence is restored. This approach provides high contrast because of the low fluorescence background of the uncleaved, inactive form. Additionally, the fluorescence signal is further amplified due to the activation of multiple probes by a single enzyme [14].

Activatable fluorescent probes have been successfully used in a wide range of small-animal imaging studies. The short penetration depth of light in tissue due to strong optical attenuation and scattering, however, limits their translation to clinical applications and leads to poor spatial resolution beyond a few millimeters [21]. Photoacoustic imaging has emerged in the last two decades as an alternative optical modality offering significantly improved resolution (up to 0.02 mm) and penetration depth (up to 5 cm) in tissue imaging [41]. Its application has been demonstrated in clinical studies for skin cancer diagnosis [71] and breast cancer screening [72].

Activatable photoacoustic probes have recently been proposed and studied by several groups [55, 56]. They rely on a change in the absorption spectrum upon activation to selectively detect the activated probe signal. This method requires multi-wavelength illumination to resolve the spectral contribution of each chromophore by linear fitting and assumes that the spectral distribution of probes and tissue absorbers is known. In practice, non-uniform light distribution due to wavelength-dependent attenuation and heterogeneous

optical properties of tissue hamper accurate spectral identification and background signal suppression.

In this work, we propose a new photoacoustic contrast mechanism that is based on switching the excited-state lifetime of the probe from short (< 100 ns) to long (> 2 μs). PLCI - a pump-probe approach that eliminates the need for spectral deconvolution by measuring lifetime contrast using only two illumination wavelengths - is applied for the first time to selectively detect the signal from activated probes.

2.2.2 *Photoacoustic lifetime contrast imaging*

Methylene blue is a planar cationic and water-soluble dye of the phenothiazine family with an absorption peak at 664 nm in its monomer form (Figure 2.2). It is commonly used, or under study, in several therapeutic and diagnostic applications [73, 74]. Both orally and intravenously administered MB are excreted by the kidneys, either unchanged or reduced to leucomethylene blue by the enzyme methemoglobin reductase present in red blood cells [75, 76]. Following optical absorption, the ground state molecule (S_0) is excited into a singlet state (S_1), and then undergoes intersystem crossing (ISC) to a metastable triplet state (T_1) with high quantum yield ($\Phi_{ISC} = 0.50$) [68] (Figure 2.3). The excited triplet state lifetime is typically tens of microseconds in an oxygen-free environment because of the spin-forbidden nature of the T_1-S_0 transition. Collisional quenching by oxygen decreases the lifetime to about 2 μs in aerated solutions at atmospheric pressure [39].

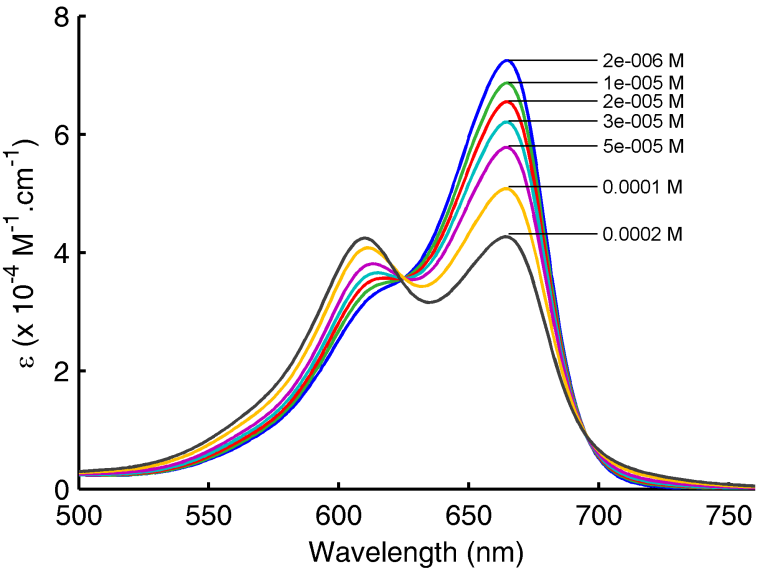

Figure 2.2. Absorption spectra of MB in water (2 µM to 200 µM). The absorption maximum shifts from 665 to 608 nm with increasing [MB] indicating an increase in the dimer-to-monomer molar ratio. The isosbestic point at 625 nm is shifted towards the blue wavelengths for MB > 100 µM due to the formation of higher order aggregates.

Molecular association between monomers occurs spontaneously in water due to a combination of hydrophobic interactions, hydrogen bonding and Van der Waals forces [77, 78]. The coupling between monomers results in a splitting of the singlet excited state into two states - of lower and upper energies – which manifests by a splitting of the absorption band of the monomer (Figure 2.3) [77, 79-81]. Figure 2.2 shows a shift in the absorption peak from 665 nm to 608 nm with increasing MB concentrations. This corresponds to the preferential transition to a higher energy state resulting in a dominant blue-shifted peak specific of H-type (or face-to-face) dimers. If a dimer is excited to the upper state S_1, it undergoes very fast (10^{-12} s) internal conversion to the lower state S_1', and, because transitions from S_1' to S_0 are forbidden, intersystem crossing is enhanced. If the coupling between monomers is strong, electron transfer is expected to occur between the pair

resulting in triplet lifetime quenching and formation of transient radical ion pairs [82, 83]. Excitation of an aqueous MB solution revealed the existence of a fast transient derived from the dimer, allegedly a triplet state, which decays into a slow transient pair formulated as a charge-transfer [84]. In an experiment mixing MB with sodium dodecyl sulfate - a compound that promotes MB dimerization at specific concentrations - Junqueira et al. reported lifetimes of 40 ns, 1.6 µs and 300 µs for the triplet, radical anion and radical cation respectively [63].

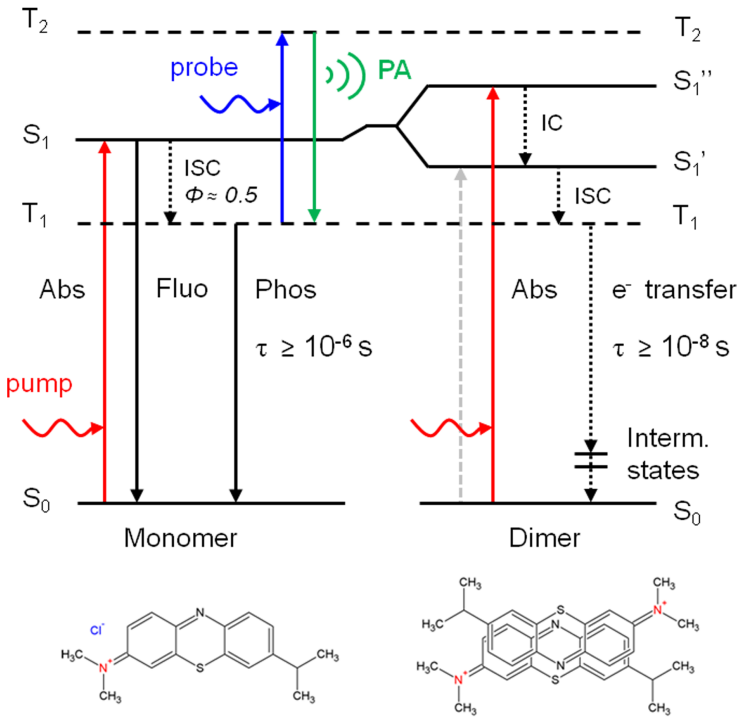

Figure 2.3. Energy diagram of MB monomer and dimer. Plain lines represent radiative transitions. Small dashed lines represent nonradiative processes. The energy of the T_1:T_2 absorption is converted into a photoacoustic relaxation signal. The double bar indicates a discontinuity in the transition diagram: the dimer triplet undergoes electron transfer (~ 40 ns) which leads to the formation of oppositely charged radicals that relax to the ground state via charge recombination (~10^{-6} to10^{-4} s). *S_0:* ground state, *S_1:* singlet excited state, *T_1:* primary triplet excited state, *T_2:* secondary triplet excited state, *S_1' and S_1'':* split exciton states, *ISC:* intersystem crossing, *IC:* internal conversion. *Bottom:* configurations of MB monomer and H-type dimer.

PLCI is a pump-probe approach that consists of applying an initial laser pulse (pump) to excite the dye to the T_1 state and a secondary pulse (probe) to excite T_1 to a T2 state resulting in ultrasound waves generated during the $T_2 \rightarrow T_1$ photoacoustic relaxation (Figure 2.3). With this technique, the amplitude of the measured photoacoustic signal corresponds to the sum of the lifetime-dependent photoacoustic relaxation - a quantity proportional to the optical absorption of the T_1 state - and the lifetime-independent background photoacoustic signal due to the excitation of the background environment by the probe pulse. By repeating a sequence of pulse pairs with different time delays between pump (dye excitation) and probe (photoacoustic wave generation) pulses, we can measure the decay dynamics of the triplet state and extract the excitation lifetime by exponential fitting. This technique has been recently demonstrated for quantitative measurement of dissolved oxygen levels in phantom objects by our research group [39].

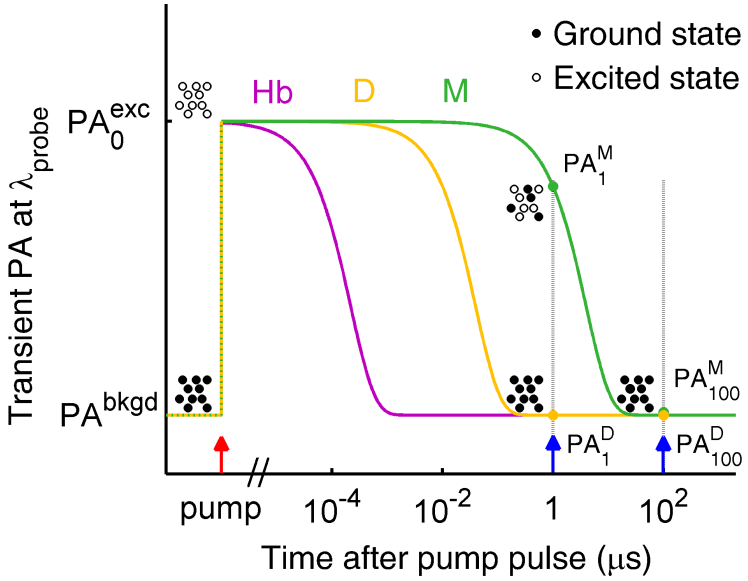

Figure 2.4. Normalized transient photoacoustic signal for MB monomer (τ = 4 μs), dimer (τ = 40 ns), and hemoglobin (τ = 0.22 ns).

The distinct separation of lifetimes between MB monomers, MB dimers, and main biological components – the lifetime of hemoglobin, albumin, myoglobin and melanin fall in the range of several tenths to several nanoseconds [59-62] – can be exploited to efficiently suppress all photoacoustic signals arising from absorbers having lifetimes shorter than a set threshold. Figure 2.4 shows the normalized photoacoustic signal of hemoglobin, MB dimers and MB monomers in low oxygen environment measured after probe excitation in a uniformly illuminated sample. Since MB monomers and dimers do not absorb at the probe wavelength (800 to 850 nm) [85], the background photoacoustic signal is constant and equal to the value after complete relaxation of the chromophores, i.e. $PA_{100\ \mu s}$. By subtracting two photoacoustic signals taken with a pump-probe delay of 1 μs and 100 μs, the only contribution comes from monomers. Additionally, dividing the difference signal by $PA_{100\ \mu s}$ normalizes the monomer signal to the probe laser energy which corrects for energy deposition fluctuations within the illuminated sample. A photoacoustic contrast parameter as defined in (1) is proportional to the monomer concentration:

$$C_{PLCI} = \frac{PA_{1\ \mu s} - PA_{100\ \mu s}}{PA_{100\ \mu s}} = \frac{PA_{monomer}}{PA_{background}} \propto [\text{monomer}] \qquad (1)$$

2.2.3 *Study goal*

The goal of this study was to investigate two dimerization models to validate the contrast mechanism between MB monomers (activated probes) and dimers (inactive probes). The first system involves sodium-sulfate-driven dimerization caused by the

increase of hydrophobic interactions with ionic strength. The second system incorporates dimerization induced by sodium dodecyl sulfate premicellar aggregates. We have used these two systems to switch between high dimer concentration and high monomer concentration, and to demonstrate that PLCI can achieve an efficient suppression of the dimer signal relative to that of the monomer.

2.2 MATERIALS AND METHODS

2.2.1 *Materials*

Methylene Blue hydrate (purum ≥ 97%), and sodium dodecyl sulfate (≥ 99.0%) were acquired from Sigma-Aldrich (St. Louis, MO) and sodium sulfate anhydrous (ACS) was acquired from Mallinckrodt Chemicals (Phillipsburg, NJ). All chemicals were dissolved without further purification in distilled water. Absorption and flash-photolysis measurements involving SDS were completed within 3 minutes after MB dilution. Experiments were performed at 22 ± 1 °C, and the pH of the solutions was measured to be within 6.7 ± 0.9. Changes in temperature and pH level in these ranges do not have a significant effect on MB dimerization.

2.2.2 *Absorption measurements*

Absorption spectra were recorded on a UV/Vis CaryUV Varian spectrophotometer using glass and plastic cuvettes of 0.1, 0.5 and 1 cm thickness. Triplet transient absorption was measured independently from PA experiments at fixed wavelengths by laser flash

photolysis. The pump pulses were generated by an optical parametric oscillator (OPO, Opotek MagicPrism) pumped by a tripled Nd:YAG pulsed laser (Surelite I-10, Continuum, f = 10 Hz, pulse width = 5 ns). The solution-filled cuvettes were probed by a laser diode (λ = 808 nm, P = 150 mW) emitting continuously at a right angle with respect to the pump laser beam. The probe beam, once transmitted through the sample, is bandpass filtered (Thorlabs, FB810-10, central frequency = 810 nm) and measured by a Si photodetector (Thorlabs, DET10A). The signal is recorded by a digital oscilloscope (Lecroy, Wavejet 354) and transferred to a computer for processing. All the experimental data were processed and analyzed with MATLAB.

2.2.3 *Photoacoustic experimental setup*

A PLCI experimental setup was used to probe the photoacoustic signal of plastic tubes filled with dye or mixed salt/dye or SDS/dye solutions as illustrated in Figure 2.5. Two tunable Nd:YAG pulsed-laser systems (Surelite I-10, Continuum; Quantel, Brilliant; both: f = 10 Hz, pulse width = 5 ns), each coupled to an OPO (Opotek MagicPrism), delivered the pump and probe pulses (6 and 8 mJ respectively). The output of both OPO systems was coupled to a bifurcated light guide (Dolan-Jenner, EE436, non-randomized for salt experiment; or Moritex, MWG-1000S-SD, randomized for SDS experiment) to ensure uniform illumination of the plastic tubes. The tubes were immersed in a water tank, and a focused ultrasound transducer (Panametrics, V382, 3.5 MHz for salt experiment; or V311, 10 MHz for SDS experiment) aligned with the incident laser beams detected the photoacoustic signals generated in the samples. Laser firing and ultrasound acquisition were synchronized by a field-programmable gate array (FPGA, KNJN, FX2 Saxo). Signals

were amplified by 50 dB (Panametrics, 5072PR), recorded by a digital oscilloscope (Lecroy Wavejet 354), and transferred to a computer for processing. B-mode images were acquired by scanning the tubes perpendicular to their long axis using a motorized actuator (T-LA28A, Zaber) mounted on a translation stage. To maximize contrast, the wavelengths of both beams were independently tuned near the maximum of absorption for the monomer and triplet species and within the range of maximal output energy for the OPOs.

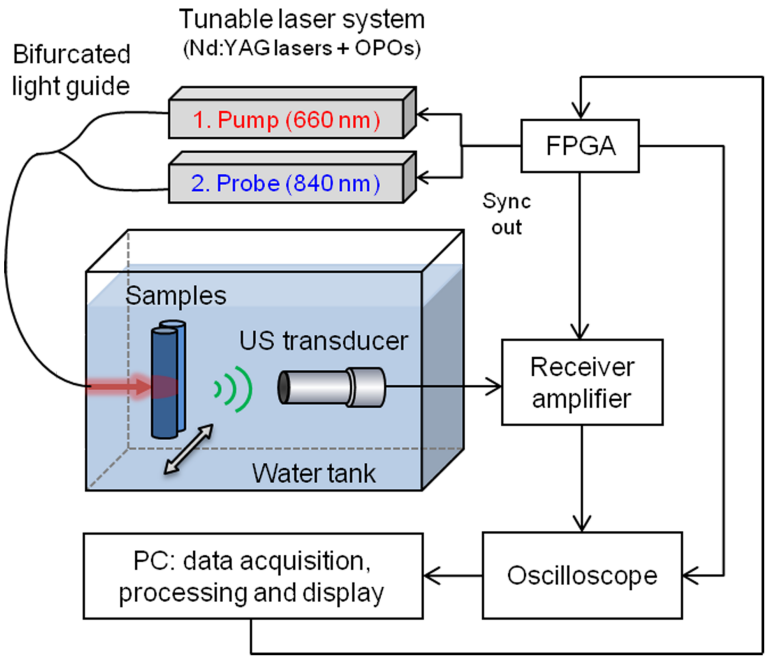

Figure 2.5. PLCI experimental setup. Pulsed outputs of the excitation laser (660 nm) and photoacoustic laser (840 nm) were combined with a bifurcated light guide and illuminate the target. The time delay between the excitation and probe pulses was controlled by an electronic synchronization circuit. The solutions were placed in two plastic tubes and scanned horizontally. The generated acoustic waves were detected by a focused ultrasound transducer. *Sync out:* synchronization output.

2.2.4 *Calculation of monomer and dimer concentrations*

The individual monomer and dimer spectra were obtained using a two-state model analysis of the spectral data in the concentration region where the monomer-dimer equilibrium is dominant (2 μM to 50 μM), as indicated by a stable isosbestic point at 625 nm (Figure 2.2). For concentrations greater than 50 μM, we observed a progressive blue shift of the isosbestic point that can be attributed to the formation of a small amount of trimers (with absorption maximum at 580 nm) [86]. In this model (adapted from Patil et al. [78]), the dimer dissociation constant K_D is defined as (2):

$$K_D = \frac{[M]^2}{[D]} = \frac{2x_M^2 C}{(1 - x_M)} \tag{2}$$

where C is the total concentration of the dye; C = [M] + 2[D], and x_M is the monomer molar fraction; x_M = [M]/C. If we assume that we have only two species in solution, then the Beer-Lambert law is applicable to those species (3):

$$A^{\lambda} = \varepsilon^{\lambda} \cdot 1 \cdot C \tag{3}$$

where the observable molar absorption coefficient ε^{λ} can be expressed as a function of the individual molar absorption coefficient of the monomer ε_M^{λ} and the dimer $\varepsilon_D^{\lambda}/2$ (4):

$$\varepsilon^{\lambda} = x_M \varepsilon_M^{\lambda} + (1 - x_M)\varepsilon_D^{\lambda} / 2 \tag{4}$$

also written in the linear form (5):

$$\varepsilon^{\lambda} = x_M * (\varepsilon_M^{\lambda} - \varepsilon_D^{\lambda} / 2) + \varepsilon_D^{\lambda} / 2 \tag{5}$$

We computed a linear regression to model the relationship between the molar absorption coefficient ε^{λ}, measured for different concentrations, and the monomer molar fraction at those concentrations to calculate the value of the dissociation constant K_D that minimizes the sum-of-squared residuals over several wavelengths. We found a K_D value of 2.6 x 10^{-4} M which is in good agreement with the value reported by Patil et al. (2.9 x 10^{-4} M, at 27 °C) and by Rabinowitch and Epstein (2.8 x 10^{-4} M, at 26.7 °C) [65].

The ε_M and $\varepsilon_D/2$ values at different wavelengths were extracted from the slope and origin of the linear fit and used to generate the individual monomer and dimer spectra (dashed lines in Figure 2.6 (a)). Assuming a two-component system, we can use a rearranged form of eq. (4) to establish a concentration-independent relationship between the dimer-to-monomer absorption peak ratio and the true monomer molar fraction (6):

$$x_M = f\left(R = \frac{\varepsilon^{\lambda_D^{max}}}{\varepsilon^{\lambda_M^{max}}}\right) = \frac{\varepsilon_D^{\lambda_D^{max}}/2 - R * \varepsilon_D^{\lambda_M^{max}}/2}{R*(\varepsilon_M^{\lambda_M^{max}} - \varepsilon_D^{\lambda_M^{max}}/2) - (\varepsilon_M^{\lambda_D^{max}} - \varepsilon_D^{\lambda_D^{max}}/2)} \quad (6)$$

2.3 RESULTS AND DISCUSSION

2.3.1 *Dimerization in sodium sulfate*

MB dimerization can be enhanced by increasing the ionic strength of the solution as accomplished by adding salts such as sodium sulfate [87]. Figure 2.6(a) represents the absorption spectra of MB 80 μM for increasing Na_2SO_4 concentrations, along with the individual monomer and dimer spectra calculated by applying a two-state model analysis

to the data obtained in water. The spectra have been normalized to the isosbestic point to compensate for small concentration variations due to dilution uncertainty, and a correction factor was calculated. The blue shift of the absorption maximum from 665 nm to 608 nm indicates that dimerization is enhanced with increasing salt concentration. The dimer peak does not exhibit a significant blue shift compared to the sole dimer spectrum (< 1 nm for $[Na_2SO_4]$ = 0.75 M), therefore we conclude that trimerization does not perturb the monomer-dimer equilibrium significantly, and we adopt the two-state model for the evaluation of the monomer fraction in each case.

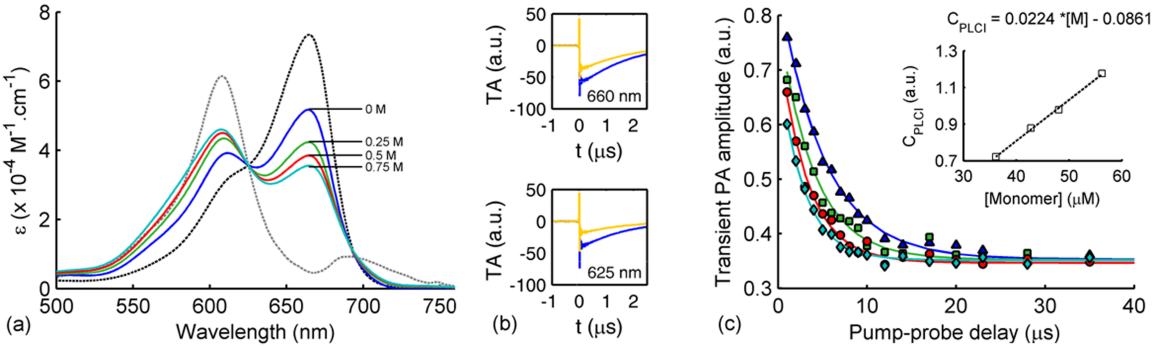

Figure 2.6. (a) Solid lines: absorption spectrum of a solution of MB 80 μM for four different salt concentrations. *Dashed lines:* individual MB monomer (black) and dimer (gray) spectra in water. (b) Transient absorption (*TA*) of a solution of MB 80 μM with (orange) and without Na_2SO_4 0.8 M (blue) measured by flash photolysis. *Top:* λ_{exc} = 660 nm. *Bottom:* λ_{exc} = 625 nm (c) Transient photoacoustic signal amplitude as a function of pump-probe delay time acquired at four different Na_2SO_4 concentrations, 0 M (Δ), 0.25 M (□), 0.5 M (○), and 0.75 M (◊). Inset: the photoacoustic contrast parameter was observed to be linearly dependent on the estimated monomer concentration (R^2 = 0.9980).

We measured the triplet transient absorption of a solution of MB 80 μM with and without Na_2SO_4 0.8 M using flash-photolysis for λ_{exc} = 660 nm (Figure 2.6(b, top) and observed that the amplitude of the signal decreases with the addition of salt while the

lifetime remains unchanged. To ensure that this decrease is not due to a difference in absorption at the excitation wavelength, the experiment was repeated for λ_{exc} = 625 nm (Figure 2.6(b), bottom) and yielded the same qualitative results. This indicates that MB dimers are statically quenched and that their triplet excited-state lifetime is short.

Finally, photoacoustic probing of the MB/salt solutions was performed in a single tube. MB monomers were excited at 660 nm, and the triplet decay was probed at 800 nm for increasing pump-probe delay times. Figure 2.6(c) shows that the amplitude of the photoacoustic signal decreases with the salt concentration, which is in agreement with the flash-photolysis results. The photoacoustic contrast parameter was calculated between 1 μs and 100 μs and plotted against the estimated monomer concentration (inset Fig. 2.6(c)) which was obtained by multiplying the monomer molar fraction by the total MB concentration adjusted by the correction factor found from the absorption spectra. C_{PLCI} at the plastic-wall interface is in linear relationship with the monomer concentration (R^2 = 0.9980). We believe that the non-zero origin may be explained by an overestimation of the monomer concentration or a difference in local light distribution between 1 μs and 100 μs.

2.3.2 *Dimerization in sodium dodecyl sulfate*

Despite their ability to increase dimer formation, salts have a limited power to overcome strong repulsive forces between MB molecules and do not induce full dimerization even at concentrations close to the solubility limit. Sodium dodecyl sulfate (SDS), on the contrary, is an anionic surfactant that binds MB due its opposite charge and provides a hydrophobic microenvironment that promotes dye aggregation on a larger scale.

SDS concentrations as low as 1 mM have been shown to significantly increase MB dimerization [63, 69, 88]. The following experiments were realized within 3 minutes after MB dilution to ensure that the solutions remained stable over time.

Absorption measurements (Figure 2.7(a)) revealed that the progressive addition of SDS to a 100 μM MB solution shifts the absorption maximum from 665 nm to 595 nm thereby revealing the formation of H-type dimers (λ_{max} = 608 nm), and even higher order aggregates with lower absorption maxima. This is paralleled by a decrease in the triplet transient absorption measured by flash photolysis for λ_{exc} = 660 nm (Figure 2.7(c)). A maximum of polymerization occurs for [28] ≈ 4 mM (Figure 2.7(b)) which corresponds to a minimum and a 25-fold decrease in the triplet transient absorption signal (Figure 2.7(c)). The same experiment conducted for λ_{exc} = 600 nm - a wavelength for which the extinction coefficient of dimers is twice the extinction coefficient of monomers - led to the same trend and a maximum of polymerization at 4 mM as well. Finally, we observed that the maximum of polymerization is invariant with respect to MB concentration by repeating the experiment for MB = 40 μM and for MB = 200 μM.

Junqueira et al. showed that the presence of increasing amounts of MB in SDS solutions decreases the critical micelle concentration (CMC) below the known CMC in water (7-8 mM) [63]. Carroll et al. demonstrated that the scattering signal from a 1 μM MB solution exhibits a strong signal for [28] = 1.5 to 4.5 mM, suggesting the presence of a large aggregate in that range [88]. Those results indicate the formation of MB-SDS clusters or premicellar aggregates before the CMC is reached. We suggest that these pre-micelles are formed by strong electrostatic interactions between anionic SDS and cationic MB with

the surfactant possibly intercalating its hydrophobic tail between adjacent MB molecules (Figure 2.7(d)). Water molecules might also help stabilize the MB/SDS complex by forming a hydrogen-bonded, shell-like structure called an "iceberg structure" [89]. The distance between MB molecules inside the pre-micelles are short (corresponding to high local concentration) which promotes dimer formation.

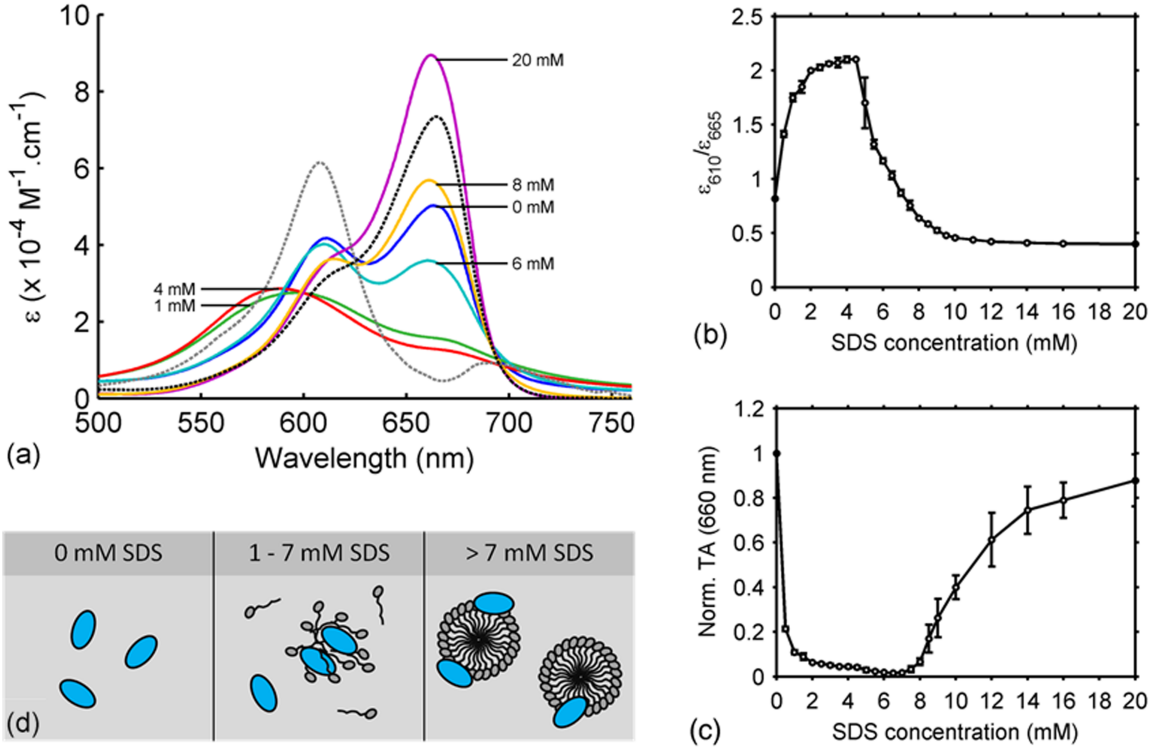

Figure 2.7. (a) Solid lines: absorption spectrum of a solution of MB 100 µM (x_M = 0.65) for six different SDS concentrations. Dashed lines: individual MB monomer (black) and dimer (gray) spectra in water. (b) Dimer-to-monomer absorption peak ratio versus SDS concentration. (c) Triplet transient absorption measured at $t = 0^+$ after excitation (660 nm) versus SDS concentration. (d) Schematic representation of MB/SDS interactions at different SDS concentrations. The data points in (b) and (c) were obtained by averaging three independent measurements and normalizing to the signal measured in the absence of SDS.

At intermediate surfactant concentrations (4.5 < [28] < 7 mM), the monomer fraction increases progressively while the triplet transient absorption remains low. Previous groups attributed this behavior to the reorganization of MB/SDS clusters as a prelude to the formation of normal micelles. During this stage, pre-micelles may be disaggregating with MB molecules released as MB/SDS quenched ion pairs [69, 88].

Finally, at SDS concentrations greater than 7 mM, the triplet transient absorption increases logarithmically until reaching a plateau corresponding to full monomerization. Concurrently, the absorption maximum at 665 nm is blue-shifted compared to the monomer spectrum, signifying that the monomers are surrounded by a more polar environment than in water without SDS (most likely the inner hydrophobic microenvironment or the negatively-charged surface of the micelle) (Figure 2.7(d)). Therefore, the increase in monomer fraction can be explained by the increase of available sites for MB molecules to bind as the number of micelles increases.

In conclusion, a SDS concentration of 4 mM effectively promotes MB polymerization by playing a cross-binding role between the dye molecules. The large extent of polymerization (more than 95 % of the initial monomers were transformed) makes this system a valuable tool for modeling the activation of a cleavable probe by photoacoustic contrast imaging.

2.3.3 *PLCI imaging between MB monomers and dimers in SDS*

Two plastic tubes respectively containing 200 μM MB + 4 mM SDS (top) and 200 μM MB (bottom) solutions were scanned by the PLCI system (Figure 2.8(a)). We estimated

that the samples contained 5 μM and 110 μM monomer concentrations respectively. For this estimation, we first determined the monomer concentration in absence of SDS by applying the methodology described in 2.2.4 to the absorption spectrum of the MB-only sample. Because the addition of SDS induces the formation of a non-negligible amount of trimers, we cannot use eq. 6 to evaluate the monomer concentration of the second sample from the absorption spectrum. Alternatively, we determined this concentration by multiplying the monomer concentration in the absence of SDS by a proportionality factor corresponding to the difference in transient absorption between the two samples obtained by flash photolysis.

The samples were probed by a 10 MHz ultrasound transducer scanned perpendicularly to the tube axis within a range of 8 mm and with step size 0.2 mm. The signals were averaged over 32 measurements to compensate for pulse-by-pulse energy variations. The scanning time was relatively short (40 minutes) such that a majority of dimers (90%) remained stable during the experiment. At each step we calculated the photoacoustic probe signal by subtracting the signal generated without the probe (excitation only) to the signal recorded with both beams (excitation + probe): $PA_{840\,(t=\tau)} = (PA_{660+840} - PA_{660})_{t=\tau}$. As ground state MB does not absorb at the probe wavelength (840 nm) [85], the signals measured at 100 μs correspond to the photoacoustic energy generated by the static background. The difference between the signal at 1 μs and the signal at 100 μs was computed to suppress the contribution of the background signal. The signals were processed with a Wiener filter followed by a low-pass filter (Butterworth, 6^{th} order, cut off frequency at 6 MHz). The envelope was detected by the Hilbert transform method.

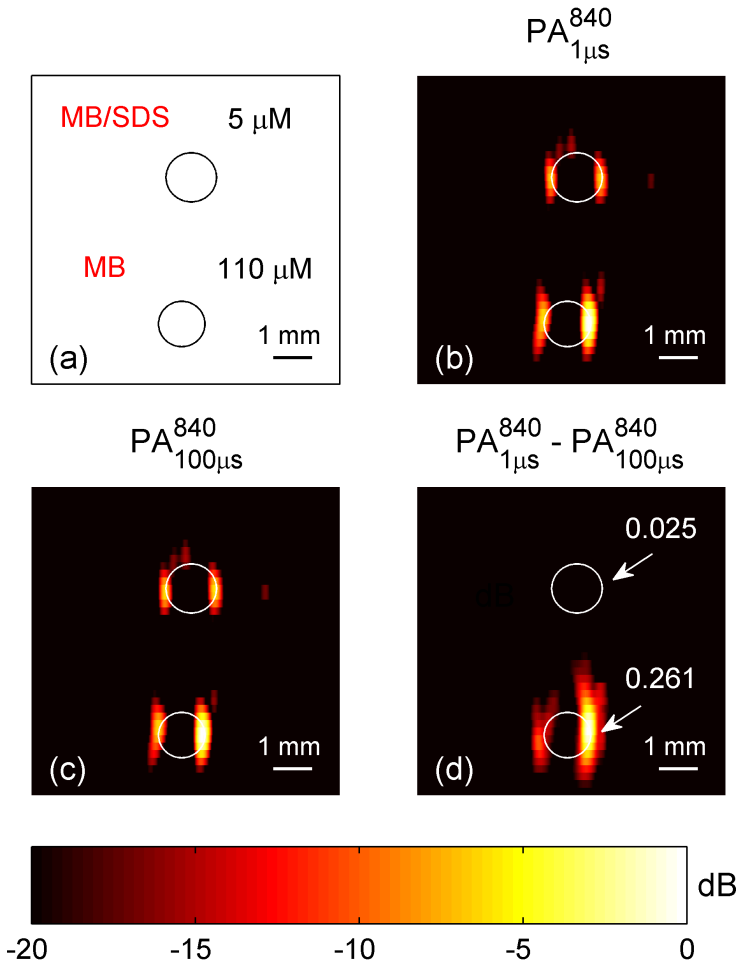

Figure 2.8. (a) Schematic representation of the position and size of the plastic tubes. Monomer concentrations are given in each case. (b) Photoacoustic amplitude image at 840 nm recorded 1 μs after the excitation pulse shows the signal generated at the plastic wall–solution interfaces. (b) Photoacoustic amplitude image at 840 nm recorded 100 μs after the excitation pulse. (d) Difference between photoacoustic amplitude images at 1 μs and 100 μs. There is a 21.5 dB suppression of the background signal due to the short lifetime of MB dimers. The numbers represent the value of the contrast parameter C_{PLCI} at the front wall of the tubes.

Photoacoustic images corresponding to 1 μs ($PA_{840\ (t = 1\ \mu s)}$) and 100 μs ($PA_{840\ (t = 100\ \mu s)}$) are displayed in Figure 2.8 on a 20 dB scale as well as their difference. The circles correspond to the location and size of the plastic tubes. Dimer and background signals are

efficiently suppressed by -21.5 dB in the differential image with a noise level of -59 dB (Figure 2.8(d)). The contrast parameter, calculated for the front wall of each tube, decreases by an average factor of 10 for the MB/SDS solution. Although C_{PLCI} is no longer proportional to the monomer concentration, possibly due to significant scattering in the MB/SDS solution, these results indicate that PLCI efficiently detects the monomer signal in a phantom object.

2.4. CONCLUSION

Here we present a new contrast mechanism for photoacoustic imaging based on the difference in excited-state lifetime between monomer and dimer forms of a chromophore. We have studied two model systems to demonstrate the sensitivity of the PLCI method to aggregation states of MB dye. The addition of salt (sodium sulfate) provides a simple and direct way to change the self-association constant of MB solution and therefore the equilibrium dimer-to-monomer ratio. We have shown that the PLCI signal depends linearly on the monomer concentration as measured by analysis of optical absorption spectra. A second model system makes use of a surfactant (SDS) to induce MB dimerization. After careful study of the system, an optimal SDS concentration was identified that results in maximal dimerization of MB. This concentration is lower than the critical micelle concentration of SDS in aqueous solution, which implies that MB-SDS aggregates form pre-micellar structures. The PLCI imaging experiment reveals a contrast of more than 20

dB between two samples of equal MB concentration, one containing free MB solution and the other containing SDS-MB for maximal MB dimerization.

Activatable smart probes have been developed as research tools for studying protein conformational dynamics [90, 91], for detecting nucleic acid hybridization [70, 92], and for sensing enzymatic activity of disease biomarkers [16, 19, 93, 94]. Based on the previous measurements, we propose a new mechanism for an activatable photoacoustic probe. In its simplest form, the probe relies on a custom-made peptide linker bearing a specific enzymatic site and confining two MB molecules to a dimer configuration. This configuration results in an intact, quenched probe of short lifetime. Reaction with endogenous enzymes cleaves the linker and separates the probe into MB monomers. The PLCI system would be used to selectively detect the long-lifetime signal from activated probes (monomers), which would provide a map of both enzyme location and activity. The lack of other long-lifetime molecules in the body empowers the sensitivity of this approach. We believe that PLCI probes could be implemented to investigate the role of specific enzymes in disease initiation and progression in animal models and establish pre-clinical data for translational research. Ultimately, PLCI probes could be developed as an early diagnosis tool and to monitor treatment efficacy.

2.5. ACKNOWLEDGEMENTS

The author is grateful to C. Sheaff for his assistance in reading the manuscript. This project was supported by NIH grant 1R21CA135027-01A1.

Chapter 3.

Engineering a Lifetime-Based Activatable Photoacoustic Probe for Matrix Metalloproteinase 2.

3.1 INTRODUCTION

Photoacoustic molecular imaging is a rapidly growing imaging modality that combines the selectivity of light-absorbing contrast agents with the relatively high spatial resolution and penetration depth of ultrasound imaging [95, 96]. Different types of photoacoustic imaging probes have been developed to visualize biological events [97, 98]. Early probe designs for cancer research have relied on passive uptake through the enhanced permeability and retention (EPR) effect to enter the tumor site [99], but they lack specificity and show high off-target signal [97]. Targeted photoacoustic probes can bind to a specific molecular marker such as cell surface receptors, transporters or enzymes, and accumulate at the target site [100], but since they continuously enable signal, they cannot provide functional information about dynamic events. A third class of photoacoustic contrast agents are activatable smart probes that can detect specific events by switching from a silent state to a detectable state upon cleavage by a target molecule, or conformational reorganization induced by environmental factors. Activatable photoacoustic probes can therefore provide low background noise and high imaging contrast [23, 61, 94, 101-108].

Recently, several groups have developed activatable smart probes for photoacoustic imaging of enzymes [23, 55, 94, 109], copper(II) [102], reactive oxygen species [110], pH

[104, 105] and temperature [106], or demonstrated the use of commercially available activatable fluorescent probes with photoacoustic detection [54, 108]. Two common methods to detect the active probe signal include single and dual wavelength imaging. Single wavelength imaging maximizes photoacoustic emission by exciting at the maximum of absorption of the active probe signal [23, 105, 106, 108]. Dual wavelength imaging relies on a change in the absorption spectrum between the inactive and active forms of the probe to enhance contrast, using either spectral subtraction [55, 94] or ratiometric detection [102, 104, 109, 110]. Both methods assume low and homogeneous absorption of background tissue absorbers and do not actively attempt to subtract the background noise. In practice, however, background absorption can vary significantly, and resolving the active probe signal may become challenging in the presence of highly absorbing and spatially heterogeneous tissue chromophores combined with low probe concentration. One strategy is to incorporate particles with high absorption capacity and high energy conversion efficiency into the probe design, such as semiconducting polymers [104, 110] or gold nanoparticles [105]. Alternatively, activated probes may be designed to aggregate locally resulting in photoacoustic signal amplification [23, 106]. Finally, Multispectral Optoacoustic Imaging (MSOT) is capable of extracting the probe signal by decomposing, or unmixing, a photoacoustic image based on the unique spectral signature of its photoabsorbing components [54]. In its simplest application, MSOT assumes prior knowledge of the absorption spectrum of each endogenous and exogenous absorber and performs a linear fit of the photoacoustic signal acquired at multiple excitation wavelengths.

Photoacoustic Lifetime Imaging (PALI) is an alternative imaging method that detects the excited-state lifetime of molecules using a two-step pump-probe approach. First, a laser pulse (pump) excites the molecule to a higher energy level. Then, a second laser pulse (probe) interrogates the optical absorption of the transient excited state by generating a transient photoacoustic signal. By scanning the time delay between the pump and probe pulses, the relaxation dynamics of this excited state can be captured. As endogenous tissue absorbers such as hemoglobin, melanin and albumin have small excited-state lifetimes in the 0.1 – 10 ns range [59-62], PALI can ignore their photoacoustic signal by suppressing any signal under a set lifetime threshold. Photosensitizers such as methylene blue (MB) and some porphyrin derivatives show potential as photoacoustic lifetime contrast agents due to their long-lived triplet excited state [111, 112] as well as their high optical absorption in the red region of the spectrum, which has reduced absorption by native molecules [113]. In addition, we have previously shown that the dimerization of MB molecules led to the quenching of their photoacoustic lifetime in sodium sulfate and sodium dodecyl sulfate solutions [114]. Here, we considered whether PALI could be employed to resolve the activation of a cleavable smart probe labeled with two MB chromophores arranged in a dimer configuration.

The probe was based on a design by Jiang et al. who developed an activatable cell-penetrating peptide for fluorescence imaging comprising an electrostatic zipper [16]. After cleavage by the target enzyme, the polyarginine half of the probe enters the cells, resulting in signal accumulation [115]. This design was later modified by Levi et. al who evaluated two chromophore-quencher pairs for dual-wavelength photoacoustic imaging [55]. More

recently, Rood et al. developed a fluorescent activatable lifetime imaging probe using luminescence quenching [116]. Our photoacoustic lifetime-based activatable probe comprises a pair of MB chromophores conjugated to an electrostatic zipper and covalently linked by the MMP-2 specific recognition sequence PLGLAG (Figure 3.1). MB dimerization is facilitated by three mechanisms: a) the PLGLAG sequence, particularly the proline and glycines, enable a substantial 'turn' in the polypeptide backbone [117]; 2. b) electrostatic attraction between the two halves of the zipper bring MB molecules together; and c) intermolecular interactions between the methylene blue moieties. Cleavage of the probe by MMP-2 enzyme separates the two halves, and the chromophores recover their long excited-state lifetime.

MMPs were chosen as a molecular target because of their role in regulating the tumor microenvironment and the signaling pathways involved in cancer progression [118]. MMPs degrade extracellular matrix proteins and various cell adhesion molecules, therefore enabling tissue remodeling during normal physiological processes and pathological states such as cancer progression and inflammation-related diseases [27, 119, 120]. Due to their ability to facilitate cell migration by rearranging the space around the cells, they are involved in tumor invasion and metastasis [121]. More recently, new roles of MMPs have been identified in tumor angiogenesis, apoptosis, inflammation, and adipogenesis, mediated by the degradation of non-matrix substrates and the release of growth factors [118]. MMPs and MMP inhibitors have been extensively studied as drug targets for cancer therapy, though treatments have yielded limited success, possibly due to the complexity of

their signaling network activity [38]. Hence, developing molecular tools to visualize MMPs is needed to better understand their role in disease initiation and progression.

In this paper, we describe the synthesis and evaluation of several conjugated agents. First, we assessed the dimerization and quenching efficiency of a pair of MB chromophores covalently linked by a single lysine. Then we compared activatable peptide probes with varying electrostatic zipper lengths and with or without a flexible linker to gain insight into their functionality.

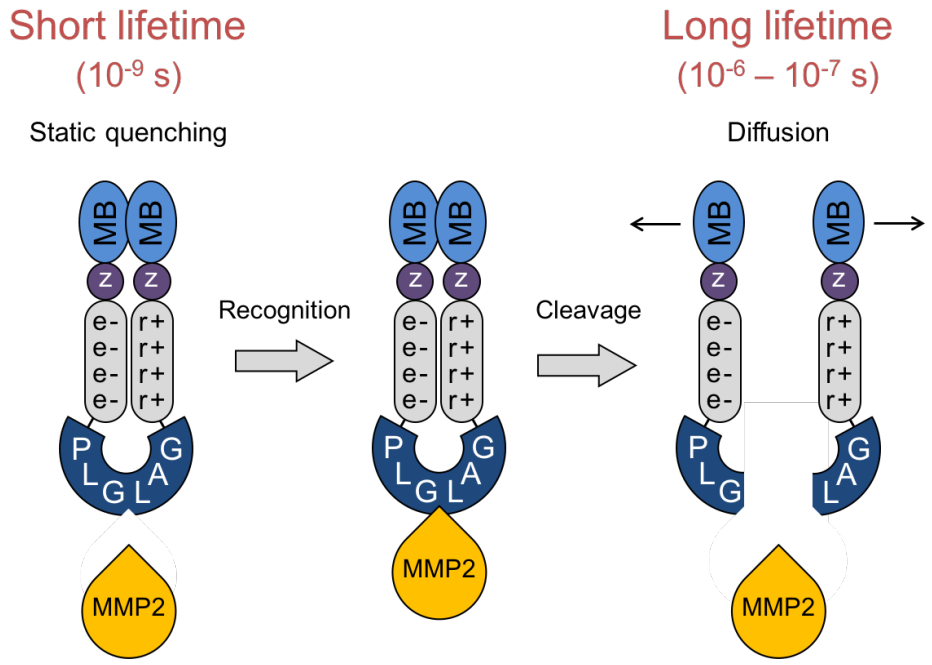

Figure 3.1. The photoacoustic probe design is composed of a MMP-2 recognition sequence PLGLAG, an electrostatic zipper comprising cationic poly-D-arginine (r+) and anionic poly-D-glutamate (e-) domains, a flexible linker (z) and a pair of MB chromophores. The intact probe is hypothesized to have a short lifetime of tens of nanoseconds due to static quenching. Upon cleavage of the recognition sequence, thereby elimination of the indirect covalent linkage, the electrostatic zipper is insufficient to maintain MB dimerization. MB monomers separate and exhibit long lifetime (1-10 microseconds).

3.2 MATERIALS AND METHODS

3.2.1 *Materials*

Methylene blue hydrate (purity ≥ 97%) and methylene blue N-hydroxysuccimide ester (MB-NHS) were acquired from Sigma-Aldrich (St. Louis, MO) and ATTO-TEC (Siegen, Germany), respectively. L-lysine was purchased from Sigma-Aldrich, and activatable peptides were purchased from United Peptide (Herndon, VA). Recombinant human MMP-2 proenzyme was from Calbiochem. *p*-aminophenylmercuric acetate (APMA) (**toxic**; use proper safety precautions) was from Sigma-Aldrich. TCNB buffer was prepared by mixing 50 mM Tris-HCl, 10 mM $CaCl_2$, 150 mM NaCl and 0.05% (w/v) Brij-35 (Technicon), and adjusting the pH to 7.5 by adding 1M HCl.

3.2.2 *Synthesis of MB-lysine conjugates*

MB-NHS ester and L-lysine were resuspended in dry DMSO to 20 mg/mL and 2.2 mg/mL, respectively. A 3-fold molar excess of L-lysine was added to the MB-NHS solution to ensure both MB-K and MB_2-K as products, along with 2% v/v trimethylamine. This mixture was left to react protected from light at room temperature for 2 hours. The samples were then purified using a C18 reverse-phase HPLC purification column with a solvent gradient of 22.5-67.5% acetonitrile in water with 0.1% trifluoroacetic acid. Individual peaks containing dually and singly labeled conjugates were collected and analyzed via electrospray ionization mass spectrometry (MALDI-TOF/TOF 5800, Applied Biosystems-Sciex Framingham, MA). Finally, the samples were lyophilized and stored at 4°C prior to testing.

3.2.3 *Synthesis of activatable peptide probes and their controls*

Peptides were resuspended in distilled water or buffer solutions of phosphate-buffered saline (PBS) and 0.2 M sodium bicarbonate (20:1 v/v) with a final pH of 8.3. To conjugate each peptide terminus with MB, a 3-6 molar excess of MB-NHS resuspended in DMSO (20 mg/mL) was added to each peptide solution and allowed to incubate for > 24 hours protected from light at room temperature. The samples were then purified via reverse-phase HPLC using C18 reverse-phase HPLC purification column with varying gradients of water/acetonitrile and 0.1% TFA. Peaks containing dually-labeled peptides were collected. Peak purity > 95% was verified via mass spectrometry, with lower purity samples undergoing further reverse-phase HPLC purification. Purified probes were lyophilized and stored at 4°C, and resuspended before use. Prior to each experiment, the absorption spectra of the probes were verified to be invariant with concentration (data not shown), indicating that no significant cleavage took place prior to enzymatic incubation.

3.2.4 *Absorbance spectra*

All MB-lysine conjugates and activatable peptide compounds were first solubilized in distilled water and then diluted to their working concentration in distilled water or PBS before testing. Absorption spectra were measured using 384-well microplates with a SpectraMax Plus 384 spectrophotometer (Molecular Devices, CA) or a Synergy H1 spectrophotometer (BioTek, VT). The pure monomer and dimer spectra were obtained from a two-state linear regression model of MB dimerization described previously [114].

Total molar concentrations were calculated using Beer Lambert's law and the extinction coefficient of MB at the isosbestic point (35,700 $M^{-1}.cm^{-1}$) calculated with this model.

3.2.5 *Enzyme kinetics*

MMP enzymes become active after cleavage of their inhibitory N-terminal domain [122]. MMP-2 proenzyme was activated by incubating a 1:9:1 v//v ratio of MMP-2, TCNB buffer and 11 mM APMA freshly dissolved in 0.1 M NaOH at 37°C for 45 minutes. All experiments performed with APMA must follow the guidelines established for using organic mercuric compounds, including wearing appropriate protective equipment. The initial activation rate of the probes was measured by incubating 10 μM peptide probe with 569 nM (0.2 ng/μL) activated MMP-2 in distilled water or in PBS at 37°C for 3 hours. We monitored the reaction by recording the absorbance at 613 nm ($\lambda_{max,\ dimer}$), 668 nm ($\lambda_{max,\ monomer}$), and 630 nm (isosbestic point) over time. Absorbances were normalized by the total concentration calculated at the isosbestic point to account for a drift in concentration over time due to evaporation. The initial rate of activation was calculated by fitting a linear regression model between the 6^{th} and 15^{th} minute, a range over which thermal stabilization was achieved. Measurements were performed three times with 2-3 replicates each time.

3.2.6 *Photoacoustic signal acquisition*

The photoacoustic experimental setup used to measure transient photoacoustic absorption was described in detail previously and reproduced in Figure 3.2(a). [114] A pump-probe system comprising two Q-Switched Nd:YAG lasers (Phocus Mobile, Opotek, and Quantel, Brilliant), each equipped with a second harmonic generator, delivered 5

nanosecond pulses at 10 Hz repetition frequency. Each beam was directed into an optical parametric oscillator (OPO; MagicPRISM, Opotek) for wavelength conversion. The pump and probe wavelengths were tuned near the maximum of absorption of MB monomers (660 nm) and the maximum of absorption of the transient excited state (830 nm) to maximize signal generation. The beams were then combined into a bifurcated randomized fiber bundle to ensure a uniform illumination of a plastic tube containing the samples. The output of the light guide was inserted into a 3D-printed photoacoustic chamber and aligned with the tube and a focused ultrasound transducer (f = 25 mm, Panametrics, V311, 10 MHz) (Figure 3.2(b)). The optical energies after the light guide were 12 and 17 mJ for the pump and probe laser, respectively. A peristaltic pump (Dolomite Microfluidics, MA) was used to draw the solutions in alignment with the light guide and the transducer. Laser firing, ultrasound acquisition, and the delay between the two pulses were controlled by MATLAB via a field-programmable gate array (FPGA, KNJN, FX2 Saxo). Pump-probe delay times were randomized to correct for time-dependent photobleaching of the solutions. The photoacoustic signal was recorded by a digital oscilloscope (Lecroy, LC584) and processed with MATLAB. Noise reduction was achieved by averaging the signal over 100 measurements during acquisition.

3.2.7 *Photoacoustic signal processing*

For each pump-probe delay time, the transient photoacoustic signal was obtained by subtracting the signal recorded with the pump laser only and the probe laser only from the signal recorded with both lasers: $tPA = PA_{660+830} - PA_{660} - PA_{830}$. The signals were then processed with a Wiener filter followed by an averaging filter. The envelope was

detected using the Hilbert transform method. Finally, the photoacoustic lifetime was evaluated by exponential fitting of the transient photoacoustic signal at the dye-plastic wall interfaces in function of pump-probe delay time.

3.2.8 *Oxygen partial pressure measurements*

The oxygen partial pressure was measured in a small volume (50 μL) of solution contained in a microcentrifuge tube using a retractable fiber-optic oxygen probe needle (OXR50, Pyroscience) and an optical oxygen meter (Firesting O2, Pyroscience). The measurements were averaged over 150 seconds after signal stabilization was reached.

3.2.9 *Statistical analysis*

An unpaired two-sampled t-test was used for statistical analysis of the probe activation data. The data were expressed as means ± standard error (SEM) from 3 repeat activation experiments using 2-3 replicates. Each repeat experiment was conducted with freshly activated MMP-2.

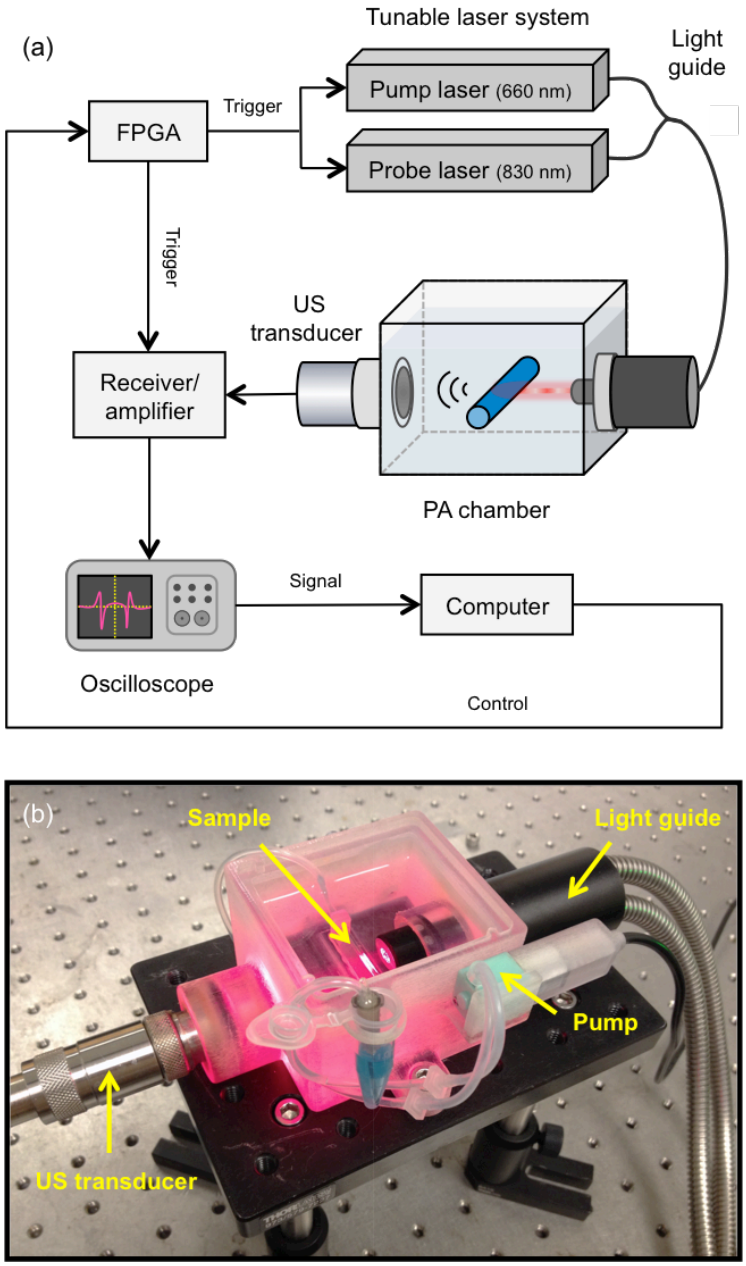

Figure 3.2. (a) Photoacoustic experimental setup. A 3D printed chamber ensures a repeatable and precise alignment between the light guide, the plastic tube filled with the sample, and the ultrasound transducer. (b) Photoacoustic chamber during laser firing.

3.3 RESULTS AND DISCUSSION

3.3.1 *Quenching of MB_2K conjugate is driven by MB dimerization*

We first tested the hypothesis that intramolecular connection of two MB molecules by a short indirect covalent link results in stable dimerization and quenching. A single lysine was chosen as the linker, and it was verified that the amino acid absorbs negligibly in the wavelength range of this experiment (data not shown). Absorbance spectra were collected for free MB, singly conjugated control MBK, dually conjugated MB_2K and hydrolyzed MB-NHS ester (MB-COOH) at different dilutions. Increasing the concentration of free MB dye results in a hypsochromic shift of the maximum of absorption from 665 nm to 608 nm as seen in sandwich-type (H-type) dimers (Figure 3.3(a)) [123]. By contrast, MB_2K displays a spectral shape that is invariant with concentration with an absorption peak at 608 nm (Figure 3.3(b)), suggesting that a single unimolecular dimer dominates the solution. To further demonstrate that this peak is caused by intramolecular MB pair interaction and not by intramolecular MB-lysine interaction, we measured the spectrum of the singly conjugated control MBK, which revealed that MBK undergoes aggregation/dissociation processes marked by a peak shift similar to that of free MB (Figure 3.3(c)). These combined results suggest that a pair of MB molecules held in close proximity by a covalent linker form a stable dimer in aqueous solution. Finally, MB-COOH dimerizes like free MB and MBK in solution (Figure 3.3(d)).

Interestingly, the absorption spectrum of MB_2K does not match the MB dimer spectrum calculated from the dimerization model used in our previous study, and exhibits

both a lower peak at 608 nm and a higher peak at 665 nm. [114] Characterization of MB_2K solution by mass spectrometry revealed that the solution contained 3% MBC-OOH, which corresponds to a MB-COOH concentration ranging from 0.80 to 3.71 μM across the dilutions – a range at which monomers represent more than 97% of all species. This would translate into a spectral decline of up to 946 $M^{-1}.cm^{-1}$ at 608 nm and a spectral rise of up to 2,060 $M^{-1}.cm^{-1}$ at 665 nm, which can only partially explain the extent of the observed deviation. An alternative explanation is that a portion (26% according to our model) of dually-conjugated MB_2K remain undimerized, resulting in a higher absorption in the monomer region. Finally, it is possible that MB_2K conjugates are completely dimerized but that their spectrum is different from that of pure MB dimer.

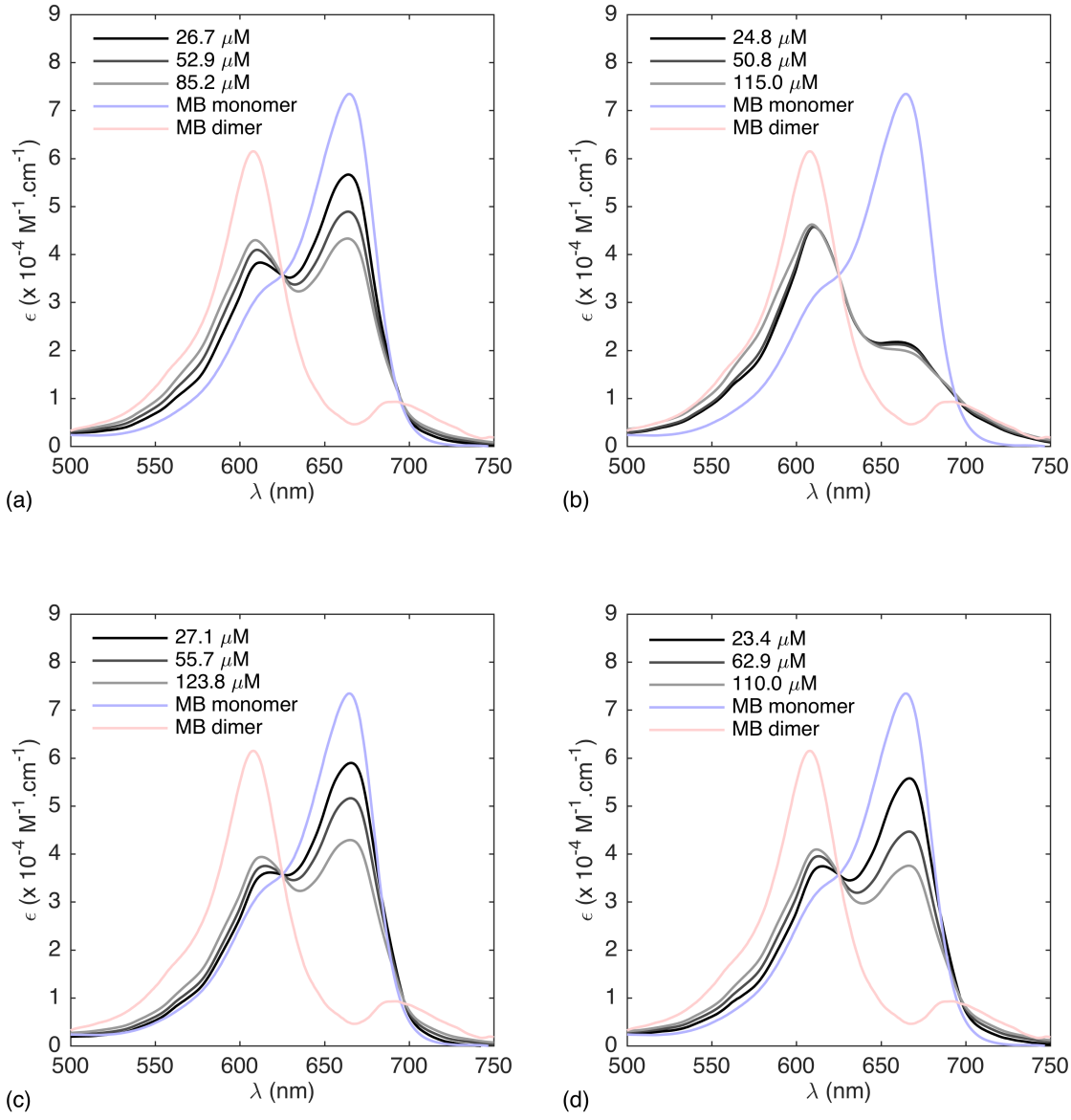

Figure 3.3. Extinction coefficient spectra of free MB dye (a), dually conjugated MB_2K (b), singly conjugated MBK (c), and MBCOOH (d) diluted at different concentrations in PBS. Dashed lines represent the pure MB.

We assessed the quenching of MBK and MB_2K by measuring their photoacoustic lifetime signal. Figure 3.4(a) shows the transient photoacoustic signal of the two conjugates for increasing pump-probe delay times (0.25, 1 and 2 μs). The back and front dye/plastic interfaces are visible at x = 0.9 mm and x = 2.6 mm, respectively. The photoacoustic

lifetime was obtained by fitting an exponential to the maximum of the PA signal in function of pump-probe delay time (Figure 3.4(b-c)). One can see that both conjugates present a photoacoustic lifetime, however the amplitude of the exponential fit decreases by 30-fold between MBK and MB_2K. The lifetimes were estimated to be 1.4 ± 0.2 µs (R^2 = 0.98 ± 0.02) for MBK and 1.0 ± 0.6 µs (R^2 = 0.81 ± 0.13) for MB_2K. The small signal observed for MB_2K may be due to the presence of a small amount of monomeric species, either in the form of MB-COOH monomers or undimerized MB_2K, however the lower R^2 values and higher standard deviation suggest that it could be the result of curve fitting error stemming from low signal-to-noise ratio (SNR). In conclusion, the decrease in lifetime amplitude for MB_2K combined with a similar photoacoustic lifetime for the two conjugates demonstrates that MB_2K is statically quenched.

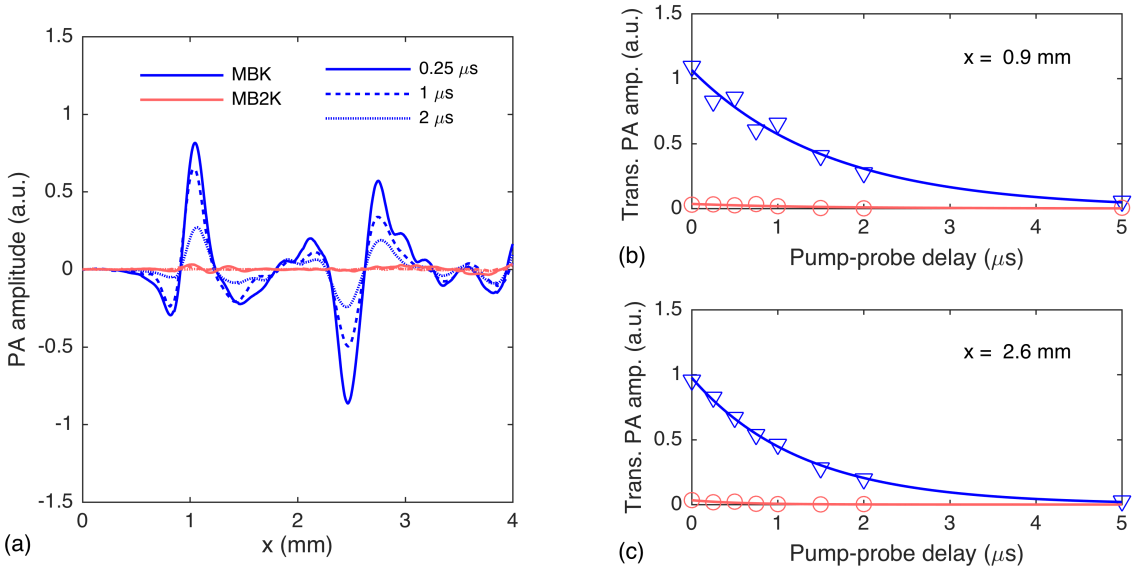

Figure 3.4. (a) Transient photoacoustic signal of a plastic tube filled with MBK (blue) and MB_2K (red) at 50 µM in 1X PBS at three different pump-probe delay times (0.25 µs, 1 µs and 2 µs). (b-c) Photoacoustic lifetime signal of MBK (▽) and MB_2K (○) solutions at the front (x = 0.9 mm) and back (x = 2.6 mm) dye-plastic interfaces. The lifetimes were calculated by applying an exponential fit to the maximum of the signal.

We previously stated the hypothesis that MB dimers have a short excited-state lifetime of a few tens of nanoseconds. However, our results do not show that MB_2K conjugates have a short lifetime component in this time range. This observation was verified by measuring the transient absorption of MB_2K with an excitation wavelength at the isosbestic point (625 nm) using flash-photolysis (data not shown). This suggests that MB_2K may not undergo intersystem crossing to a triplet state but another type of de-excitation process such as direct relaxation from the singlet to the ground state.

3.3.2 *Photoacoustic activatable probe design*

We compared the basic functionality of 12 activatable peptide probes with general structure MB-K*z*(e)$_n$[Ahx]PLGLAG(r)$_m$*z*K-MB, as well as a pre-activated and non-activatable controls (Table 3.1). We studied the effect of varying the length of the electrostatic zipper ((e)$_n$(r)$_m$) and introducing a flexible linker (*z*) on dimerization/separation efficiency and activation rate to identify the optimal probe sequence. Finally, we measured the lifetime contrast before and after incubation with MMP-2 to determine the photoacoustic quenching efficiency of the activatable probes.

3.3.3 *Validation of E4R5 activation*

The E4R5 probe was activated by MMP-2 over the course of 2.5 hours (Figure 3.5(a)). The absorption peak shifts from a state consistent with dimerization to a state consistent with monomerization, indicating cleavage. The maximum of absorption of the uncleaved and cleaved form of the probes were red-shifted by about 4 nm compared to free MB dye. The activation was monitored at 613 and 668 nm (Figure 3.5(b)).

Probe	*n* (e-)	*m* (r+)	*z*	*Targeting sequence*
E4	4	-	-	PLG
R5	-	5	-	LAG
E0R0	0	0	-	PLGLAG
E0R1	0	1	-	PLGLAG
E1R2	1	2	-	PLGLAG
E2R3	2	3	-	PLGLAG
E3R4	3	4	-	PLGLAG
E4R4	4	4	-	PLGLAG
E4R5	4	5	-	PLGLAG
E5R6	5	6	-	PLGLAG
E4DR5	4	5	-	plglag
E4scrR5	4	5	-	Pgallg
GE4R5G	4	5	G	PLGLAG
XE3R4X	3	4	[Ahx]	PLGLAG
XE4R5X	4	5	[Ahx]	PLGLAG
XE5R6X	5	6	[Ahx]	PLGLAG

Table 3.1. Designs of the activatable probe sequences of the general form MB-Kz(e)$_n$[Ahx]PLGLAG(r)$_m$zK-MB, where *n* represents the number of D-amino glutamic acids, *m* represents the number of D-amino arginines, and *z* represents a flexible linker (G, 6-aminohexanoic acid [Ahx], or none). A simplified naming convention (zEnRmz) is used to describe the different probe designs. Pre-activated positive controls are identified as E4 and R5. Negative D-amino and scrambled controls are identified as E4DR5 and E4scrR5, respectively.

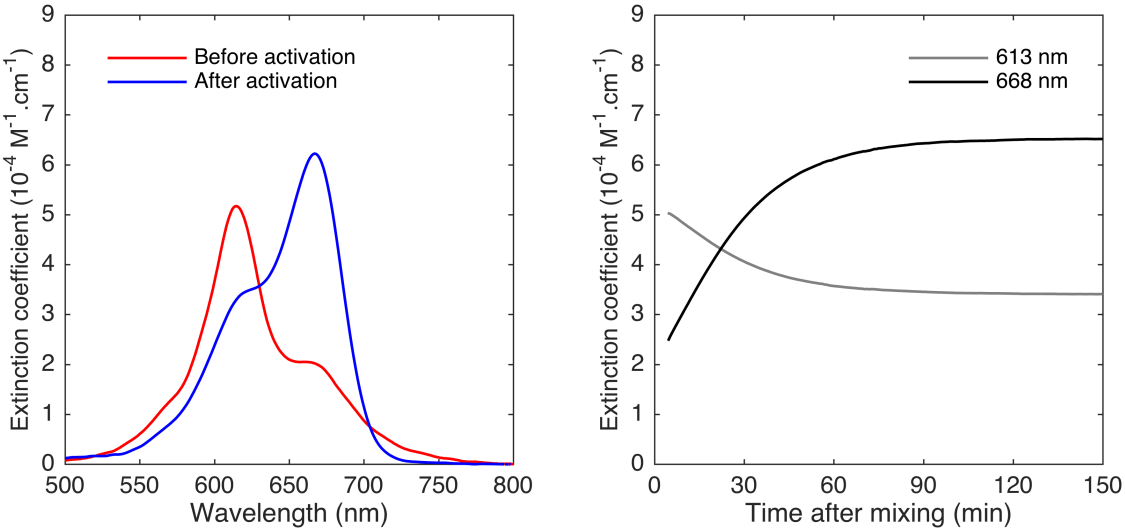

Figure 3.5. (a) Absorption spectra of E4R5 probe (10 μM) before and after incubation with MMP-2 (0.2 ng/μL) for three hours. (b) Absorption change throughout incubation measured at 613 and 668 nm.

3.3.4 *Comparison of activatable peptide probes to optimize imaging contrast*

In order to enlighten the structure/function relationship and identify the optimal probe, we compared the dimerization state and quenching efficiency of the different probes before and after incubation with MMP-2.

Before MMP-2 treatment, dually conjugated probes consistently showed a dominant absorption peak in the dimer region (data not shown) though dimerization efficiencies vary amongst designs (Figure 3.6). E3R4, E4R5 and E5R6 probes displayed a higher dimer-to-monomer ratio (D:M) than their counterparts with a G or a X linker ($P < 0.0001$ for each comparison). Furthermore, the D:M decreased significantly with linker size when comparing probes of the same zipper length ($D:M_{E4R5} > D:M_{GE4R5G} > D:M_{XE4R5X}$) ($P = 0.00006$ for both comparisons). These results indicate a size-dependent disruption of MB dimerization by flexible linkers, which we posit may be mediated either

by increased conformational freedom or by increased distance between the chromophores. Additionally, whereas the D:M did not differ significantly between E0R1, E2R3, E3R4, E4R5 and E5R6 probes, the D:M of XE*n*R*m*X probes was inversely related to their length ($r = 0.998$, $P = 0.04$). This suggests that flexible linkers may counteract the electrostatic attraction of the zipper. On the other end, the zipper-free E0R0 probe displayed a 10% lower D:M than other E*n*R*m* probes apart from E1R2 ($P < 0.001$ for each comparison), highlighting the role of the zipper in facilitating MB dimerization through electrostatic attraction of the two halves of the probe, increased conformational flexibility, or both. Finally, the D:M of E4R5 probe and its non-activatable D-amino and scrambled controls E4DR5 and E4scrR5 were not found to be significantly different ($P > 0.001$), which indicates some level of latitude in modification of the recognition sequence without impacting dimerization.

Incubation of E*n*R*m* probes with MMP-2 led to an 80 % average decrease in D:M with a final D:M comparable to that of split controls E4 + R5, indicating a complete separation of MB chromophores. In comparison, the non-activatable controls E4DR5 and E4scrR5 exhibit greatly reduced change in D:M (approximately 10 %), which supports the notion that the PLGLAG recognition sequence enables MMP-2 cleavage. The small change may indicate that cleavage took place to a lower extent over the incubation period, possibly due to enzymatic action or to reaction conditions. GE4R5G and XE*n*R*m*X probes showed a higher D:R than E*n*R*m* probes (except E5R6) after MMP-2 treatment ($P < 0.001$). We posit that the presence of a linker may partially hamper the separation of the probes or that the linker impacts MB's absorption spectrum.

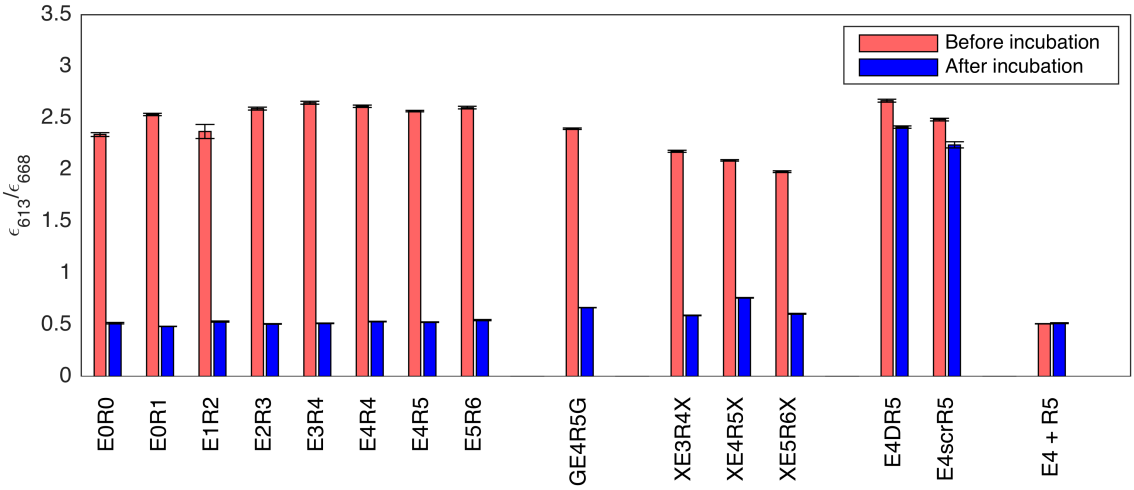

Figure 3.6. Mean (± SEM) of the dimer-to-monomer absorption ratio (D:M) of the peptide probes (10 μM) before and after incubation with MMP-2 (0.2 ng/μL) for three hours.

Two cleavable probes (E2R3 and E4R5) as well as the split and scrambled controls were assessed for their quenching efficiency (Figure 3.7). After MMP-2 treatment, the photoacoustic lifetime amplitude increased by 6- and 260-fold for E4R5 and E2R3, respectively (Figure 3.7(a-b)), although it was slightly higher for E4R5 than for E2R3 before incubation. This may be partially explained by the presence of a small amount of pre-cleaved E4R5 before adding the enzyme, which is supported by a greater monomer absorption peak for E4R5 (data not shown). In addition, the difference may be explained by the uncertainty associated with the exponential fit before incubation due to low SNR, which translates into the low R^2 presented below. The scrambled control retained a low photoacoustic lifetime signal before and after enzymatic incubation (Figure 7d), whereas that of the split control remained high, although with an 18% decrease after incubation (Figure 3.7(c)).

Interestingly, the lifetime of the split controls was found to be reduced by half (from 1.56 μs to 0.76 μs) after incubation. We tested the hypothesis that this difference may be caused by an increase in collisional quenching between MB molecules and oxygen by measuring the oxygen partial pressure (pO_2) in E4 + R5 before and after incubation (Table 3.2). pO_2 was slightly lower after incubation, which would translate into an increase in photoacoustic lifetime. However, the measured lifetime was lower after incubation, which contradicts our hypothesis. We also tested the influence of TCNB incubation buffer and NaOH on the photoacoustic lifetime of E4 + R5 (Figure 3.8), but did not observe a change comparable to the one seen after enzymatic incubation. From these results, we posit that the lifetime difference before/after activation may be due to heating during the incubation process or to the presence of APMA or MMP-2.

Probe	**pO_2**	**τ (μs) – (R^2)**
Before incubation	120 mmHg	2.5 (0.918)
After incubation	107 mmHg	0.87 (0.903)

Table 3.2. Oxygen partial pressure measured in E4 + R5 solutions (50 μM) before and after activation incubation with MMP-2 (2 ng/μL) for one hour. We tested the hypothesis that this difference may be caused by an increase in collisional quenching between MB molecules and oxygen by measuring the oxygen partial pressure (pO_2) in E4 + R5 before and after incubation. pO_2 was slightly lower after incubation (107 mmHg vs 120 mmHg), which would translate into an increase in photoacoustic lifetime. However, the measured lifetime was lower after incubation, which contradicts our hypothesis.

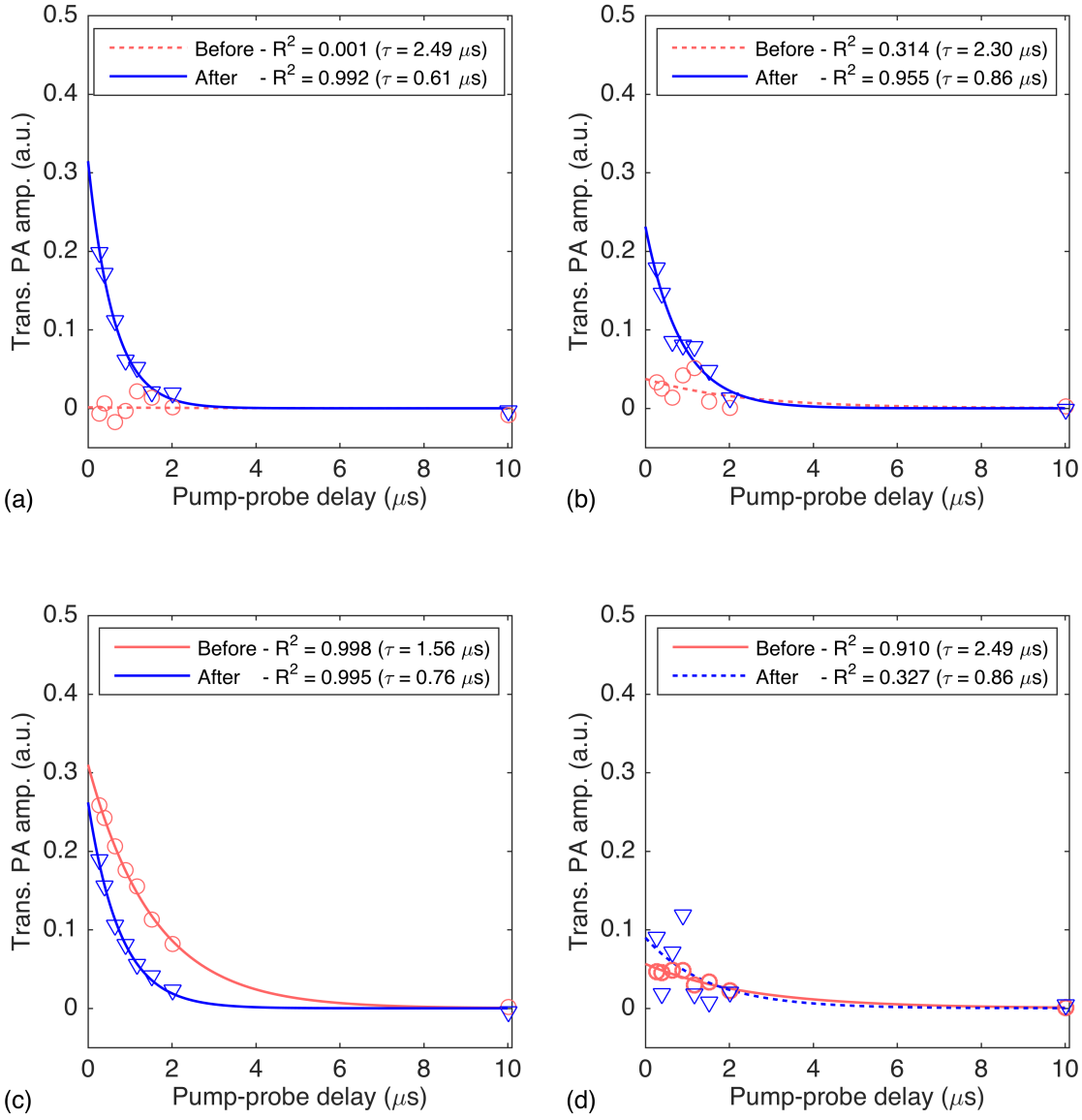

Figure 3.7. Photoacoustic lifetime signal of the back of a plastic tube filled with E2R3 (a), E4R5 (b), E4 + R5 (c) and E4scrR5 (d) solutions at 50 μM before (○) and after (▽) incubation with MMP-2 (2 ng/μL) for one hour. The lifetimes were calculated by applying an exponential fit to the maximum of the envelope signal. Dashed lines represent fits with $R^2 < 0.5$.

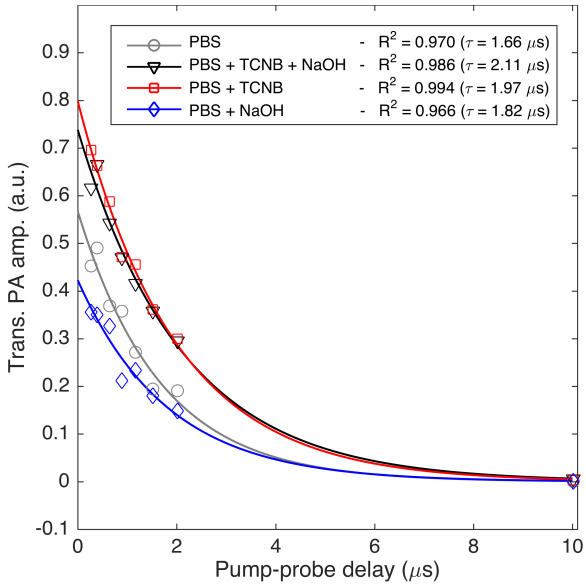

Figure 3.8. Photoacoustic lifetime signal of E4 + R5 solution (50 μM) in 1X PBS buffer (○), PBS + TCNB + NaOH (▽), PBS + TCNB (□), and PBS + NaOH (◇). The different solutions were mixed according to their relative volume fractions in the activation buffer. The addition of TCNB and NaOH separately or simultaneously did not result in a decrease in photoacoustic lifetime as observed after enzymatic incubation.

In vivo imaging of enzyme activity using an activatable probe requires high contrast differentiation between the inactive and active state of the probe. The preceding results indicate that this condition is best satisfied by a probe with MB directly conjugated to the terminal lysines *(i.e.* without a flexible linker) due to their high dimerization and self-quenching efficiency before cleavage, and high separation efficiency and photoacoustic lifetime signal after cleavage. Probes with an electrostatic zipper exhibited superior D:M ratio than the zipperless design, but extended length of the electrostatic zipper was not found to significantly impact dimerization and separation efficiency. Notably, after cleavage, one of the monomers contains a polyarginine segment, which could enable cell penetration and accumulation of half the probe in cells expressing or proximal to MMP-2 [16].

3.3.5 *Comparison of activation rate between peptide probes*

In order to more finely investigate the influence of probe structure on its attachment/separation after cleavage, we compared the initial activation rate of the probes incubated with MMP-2 and in distilled water.

The initial rate of activation (V_0) was 20 to 33 times higher in activatable probes incubated with the enzyme than in those incubated in distilled water (Figure 3.9). In addition, no significant difference was found between activatable probes and the negative controls in the absence of MMP-2 ($P > 0.1$). These results suggest that most of the cleavage is due to enzymatic activity and not to spontaneous separation of the MB moieties or non-specific proteolytic cleavage. Moreover, the initial rates for E4DR5 and E4scrR5 controls were essentially the same with and without enzyme ($P > 0.1$), indicating that the D:R change observed for these controls is likely due to incubation conditions and not to enzymatic action.

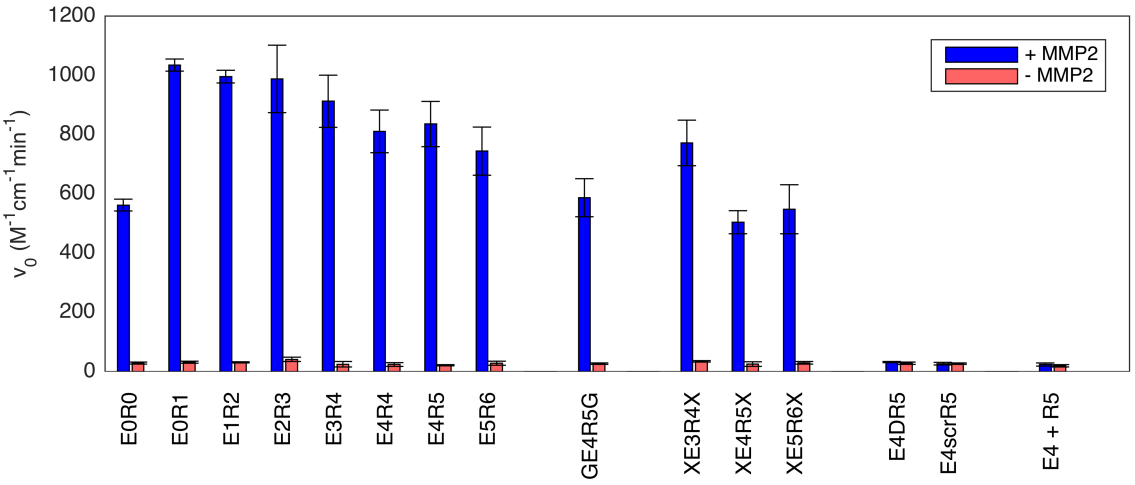

Figure 3.9. Mean (± SEM) of the nitial rate of activation of the peptide probes (10 μM) incubated with and without MMP-2 (0.2 ng/μL) for three hours.

Apart from E0R0, the activation rate of linkerless probes – but not that of XE_mR_nX probes – was found to decrease with peptide length when incubated with MMP-2. This dependence may be explained by an increase in binding affinity of the zipper side chains with length that would delay their separation after probe cleavage, or by side chain impact on the local conformation and accessibility of the cleavage site. The lower rate calculated for E0R0 may be due to a modified conformation of the cleavage site in the absence of a substantial linker between MB dimer and the protease recognition sequence. Additionally, V_0 decreased with linker size when comparing probes of the same length ($V_{0,E4R5} > V_{0,GE4R5G} > V_{0,XE4R5X}$), however we did not find the difference between probes to be statistically significant ($P > 0.05$).

In vitro testing of a smart probe's activation rate does not directly translate into in vivo probe behavior due to the complexity of live biological processes, but choosing a probe with an adequate activation rate and low non-specific activation provides some advantages. Because MMP enzymes can sometimes be found in the bloodstream [124], some level of activation in the blood and accumulation into tissue or clearance organs may occur, which could lead to off-tumor signal. Another level of complexity comes with probe specificity towards different enzymes, particularly those from the MMP family, which presents similar three-dimensional structures and substrate specificity [125]. One study comparing the sensitivity of the PLGLAG sequence to different enzymes found it to be mostly cleaved by MMP-2 and -9, and, to a lesser extent, by MMP-14 [115]. Since different tumor sites secrete different enzymes at different stages of cancer progression [27], the tumor enzymatic profile must be carefully considered when imaging an enzyme-specific

probe in vivo. For example, the expression and activity of MMP-2 secreted by prostate cancer tumors is not the same at the early and advanced stage, and higher plasma MMP-2 activity levels were correlated with invasive and metastatic behavior [126]. This property may be exploited for cancer diagnosis and/or prognosis, by tailoring an activatable probe to an enzyme whose activity is upregulated during a specific stage of cancer progression.

3.4 CONCLUSION

We have demonstrated the design and *in vitro* characterization of the first activatable photoacoustic lifetime probe. We have showed that a pair of MB chromophores linked via an enzyme-cleavable polypeptide dimerize and that their photoacoustic lifetime signal is suppressed due to self-quenching. The MMP-2 driven cleavage of the covalent linkage indirectly connecting the MB moieties results in probe separation and detection of microsecond photoacoustic lifetime signal. We have determined that probes without a flexible linker dimerize better before activation, which may translate into lower non-target signal *in vivo*, and less after cleavage, which would allow for a greater contrast. Finally, we have showed that the initial activation rate is decreasing with peptide length in linkerless probes. Other validation criteria for the probe may be tested in the future, such as cellular uptake, enzyme specificity, stability in the blood and toxicity to the cells. Moreover, the probe design can be adapted for testing a variety of biological and disease molecular markers, both enzyme and DNA-based, by changing its recognition site sequence. Potential applications in the field of molecular imaging include enzyme-targeted drug research, cancer and inflammation-related disease diagnosis, and planning and monitoring of treatment efficacy.

3.5 ACKNOWLEDGEMENTS

This project was supported by NIH grant 1R21CA135027-01A1, the Interdisciplinary Doctoral Fellowship and the Doctoral Dissertation Fellowship from the University of the Minnesota, and the U.S. Department of Veterans Affairs.

Chapter 4. Towards in vivo imaging

Development of a multimodal US/PA/PALI imaging system

4.1 INTRODUCTION

A new multimodal imaging system (US/PA/PALI) is under development at the Photoacoustics and Ultrasound lab at the University of Minnesota. The end goal is to integrate a dual-wavelength pulsed laser system, a bifurcated optical fiber for light delivery, and an ultrasound imaging probe into a portable imaging system for clinical use. A computer was programmed for data acquisition, reconstruction and real-time display of PALI functional information co-registered with anatomical ultrasound images. This chapter introduces the current imaging setup and the image formation process based on event-driven programming using MATLAB – including acquisition, reconstruction and processing steps. We demonstrate the capability of our system by imaging a plastic tube filled with MB solution and show a good overlay between the PA and US signal. Then we describe a preliminary experiment conducted on a euthanized mouse whose hindlimb was injected with MB dye and imaged by our system. Lastly, we present several improvement ideas for the imaging setup and discuss the challenges in implementing this technique in living subjects. Application of this imaging system with the photoacoustic activatable probe described in Chapter 3 would yield a map of target enzyme activity and oxygen partial pressure in tissue. This could be used by physicians to monitor the effect of a treatment on oxygen and enzymatic biomarkers and establish clinical endpoints.

4.2 METHODS

4.2.1 *Imaging setup*

The multimodal imaging system is composed of a research ultrasound (US) system (Vantage 64, Verasonics), two tunable pulsed laser systems (Phocus Mobile, OPOTEK), a Windows computer, and a FPGA-based synchronization box (Figure 4.1). The US system is connected to a 64-channel phased array transducer (P7-4, ATL) with 5 MHz center frequency and 3 MHz bandwidth. The transducer functions as a transmitter-receiver in pulse-echo US imaging mode and as a receiver only in PA/PALI imaging. The Verasonics clock output (15.625 MHz) is used as the common synchronization signal for laser firing and signal acquisition. The exact timing between pump and probe pulses and the start of the acquisition is programmed into the FPGA contained in the synchronization box (EP3C5, ALTERA Cyclone III series). The output laser beams are homogenized in a bifurcated fiber bundle and delivered to the imaging target as a slowly diverging beam (ø 5.45 mm - NA = 0.22). Independent wavelength tuning is performed by an optical parametric oscillator (OPOTEK) within the laser system enclosure. The US transducer and the fiber bundle are first manually aligned with the imaging target, then the position of the transducer is adjusted so that the field of view is centered on the target by observing real-time US images displayed on the computer.

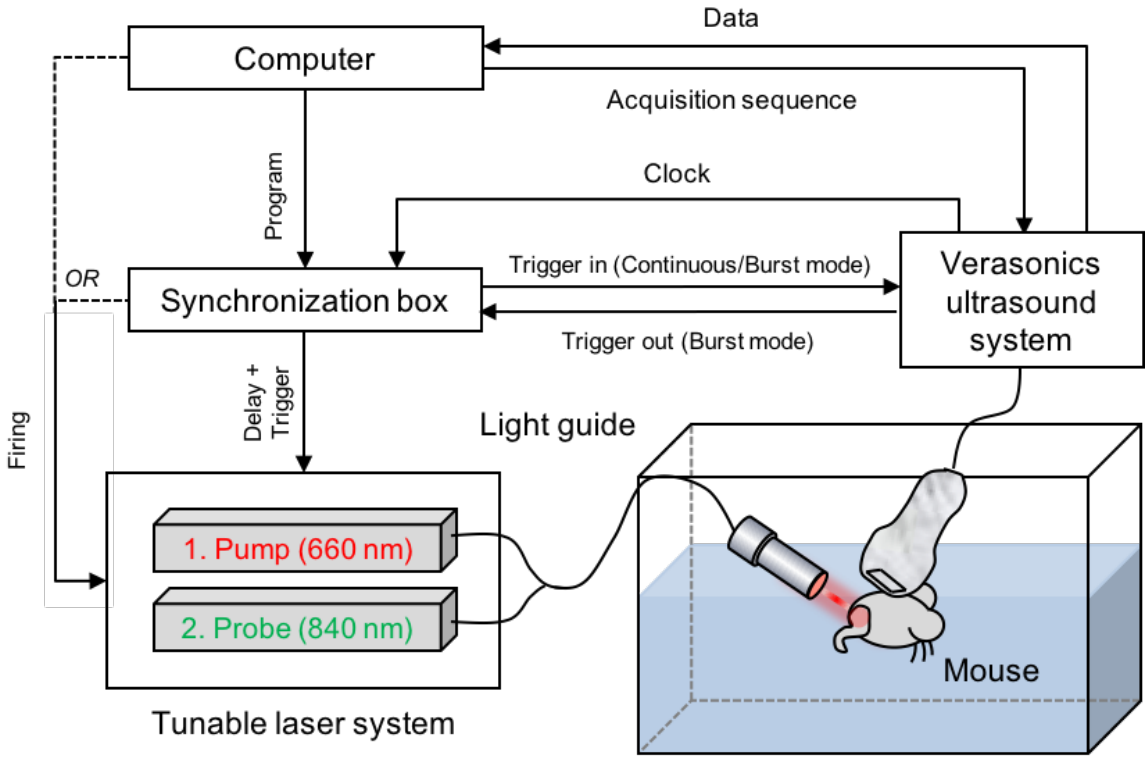

Figure 4.1. Multimodal imaging system setup. The Verasonics imaging system sets the clock (15.625 MHz) of the synchronization box which sets the time delay between the pump and probe pulses and triggers laser firing and ultrasound acquisition. The two lasers can be fired either by the computer (continuous mode) or the synchronization box (burst mode). A phased-array transducer records US and PA measurements. The data is then amplified, digitized, eventually displayed, and stored in the Verasonics system. Finally, the data can be transferred to the computer for image reconstruction and processing.

4.2.2 *Image acquisition*

Image acquisition can be programmed by writing a MATLAB script containing a sequence of actions, referred to as events, in both the hardware and software environment. There are four types of events: Transmit, Receive, Reconstruct, Process and Control. A script also generates a collection of objects, in the form of structures, which specify a set of attributes used during the sequence of events. A typical example is the transducer object,

with structure ‘Trans’, and attributes ‘name’, ‘frequency’ and ‘type’. When the setup script executes, the sequence of events loads into both the hardware and software sequencers and the acquisition starts. Asynchronous programming between hardware and software events was implemented to optimize the acquisition speed and the frame rate for real-time display.

A US imaging script starts by specifying the transmit (e.g. waveform and beam characteristics) and receive (e.g. time gain compensation and apodization) objects. For PA imaging, the transmit object can be left unfilled or the transmit apodization set to zero. In all subsequent imaging experiments, US images were acquired by the synthetic transmit aperture (STA) technique [127, 128]. This technique provides full dynamic focusing both in transmit and receive modes, yielding high-resolution images. At each step, a single element transmits an ultrasound pulse and the echo signal is recorded by all the receiving elements. The step is repeated for each of the 64 transmit channels. PA images were acquired by receiving on all elements simultaneously following laser firing. The signal was averaged 100 times for both US and PA imaging and the RF data was saved into local memory. US acquisition lasted less than a second and the full PALI acquisition for a set of 9 pump-probe time delays took about 3 minutes.

The main attributes within the setup script that can be used to optimize image acquisition are represented in blue during the acquisition step in Figure 4.2. Those are the TGC amplification waveform, the anti-aliasing filter, the low pass filter, and the decimation rate. The transmit and receive structures can also be modified to evaluate different beamforming techniques.

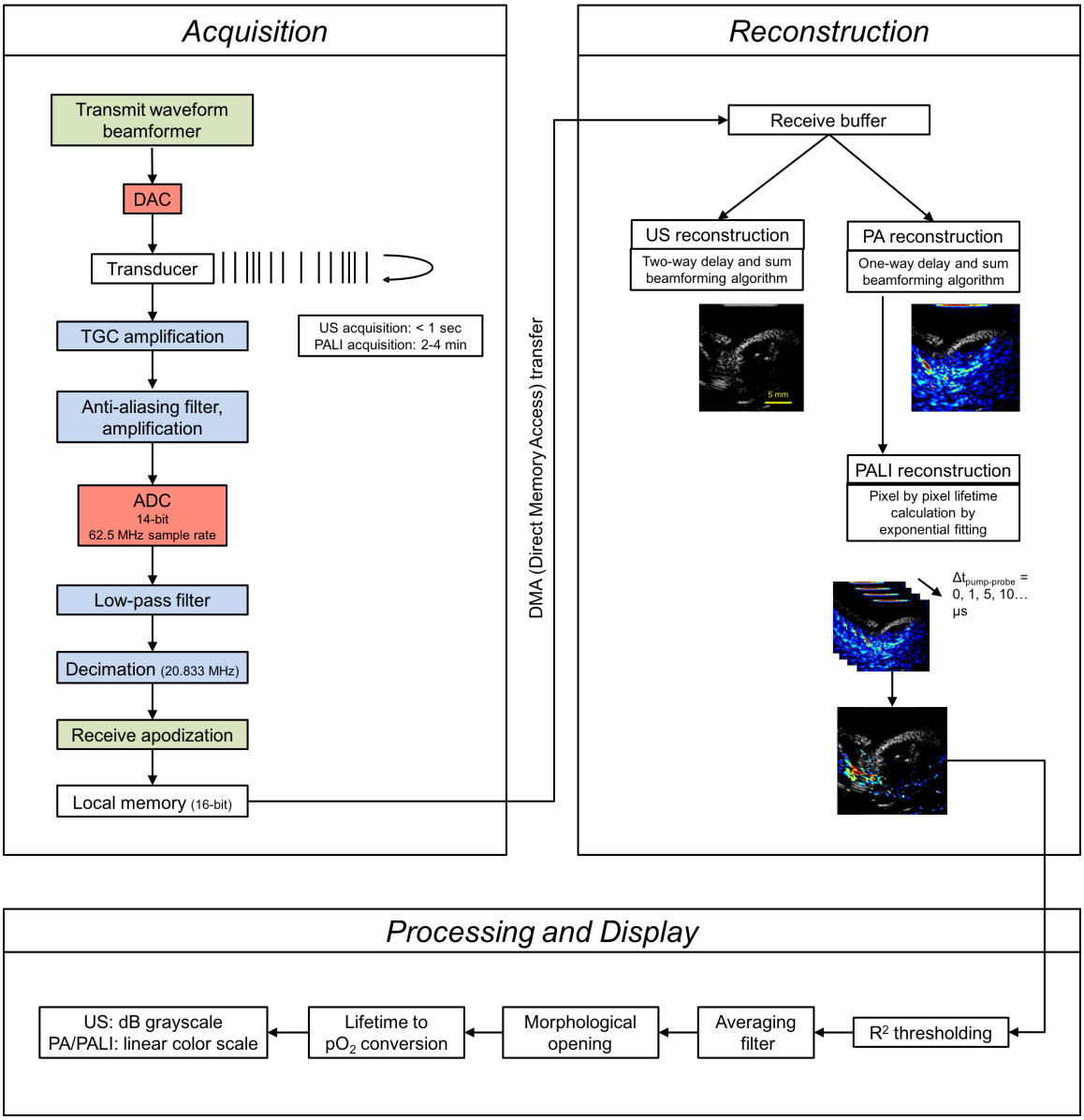

Figure 4.2. Schematics of the image formation process. *DAC*: Digital-to-analog. *ADC*: Analog-to-digital.

4.2.3 *Image Reconstruction and Processing*

The execution script can reconstruct an image in real-time using a delay and sum algorithm and display it on the computer screen through a graphical user interface (GUI). The user can specify the sensitivity cutoff in one of the reconstruction objects and set the

gain and the compression level during processing. However, for better control of the reconstruction parameters and to perform coherent subtraction of PA images for PALI reconstruction, we chose to apply our own reconstruction algorithms (Figure 4.2).

At the end of an acquisition event, the RF data is transferred to the computer and stored in a receive buffer. For each receiving element, an amplitude image was reconstructed by the delay-and-sum method (two-way for US, one-way for PA). These images were then summed up coherently and their envelope was detected by the Hilbert transform method along the axial direction. To obtain PALI images, each pixel of a series of PA images acquired for different pump-probe time delays was fit to an exponential, and pixels with a goodness of fit parameter R^2 lower than a set threshold (typically 0.9) were rejected. Finally, an averaging filter was applied to filter out high frequencies and a morphological opening operation was performed to remove isolated pixels to improve visualization. Finally, US and PALI information was co-registered and displayed on the same image with different colormaps.

4.2.4 *Phantom experiment*

Methylene blue (MB) hydrate (purity ≥ 97%) solution was dissolved to 100 μM and flown through a plastic tube placed in front of the fiber bundle inside a water tank. The fiber bundle and US tranducer positions were adjusted so that the fiber bundle illuminated the tube homogeneously and the tube was in the center of the transducer's field of view approximately 1 cm from its surface.

4.2.5 *Animal preparation*

White mice were euthanized by CO_2 inhalation at the Research Animal Ressources (RAR) at the University of Minnesota and immediately brought to the PUL laboratory. The area of the hindlimb was shaved and injected with MB (2mM – 0.5 mL) dissolved in physiological saline (PBS 1X, Mediatech) intramuscularly. The mice were then affixed to an imaging platform placed in a water tank, and the US transducer and the fiber bundle were aligned with the stained area with an 80° angle between them (Figure 4.3).

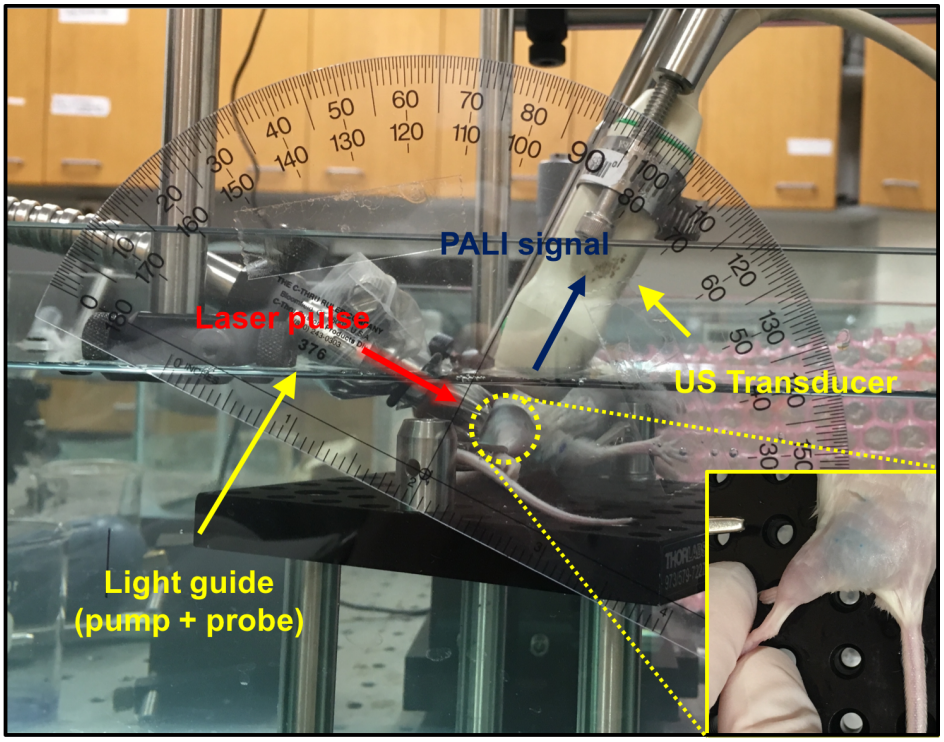

Figure 4.3. Example of an imaging platform for small animal imaging. The mouse used in this experiment has been euthanized prior to MB injection to the hindlimb and transfer to the imaging setup. The mouse was fixed to a small optical breadboard and submerged in water (in a live experiment the head of the mouse would be above water level). The stained area is illuminated by a randomized lightguide with a small ziploc bag at the tip to protect it from water. The phased-array transducer was positioned above the stained area and aligned with the illumination spot using a MATLAB script displaying the PA image in real time.

4.3 RESULTS

4.3.1 *Phantom imaging*

In order to demonstrate the capability of multimodal imaging, we imaged a plastic tube filled with MB solution. The US image was displayed in dB scale (Figure 4.3(a)), and the PA images with only the pump laser (660 nm, Figure 4.3(b)) and only the probe laser (830 nm, Figure 4.3(c)) in colorscale. The two PA signals represent the location of the plastic wall-solution interface, and overlap nicely with the US image. The PA signal at 660 nm corresponds to the absorption of MB monomers, whereas the PA signal at 830 nm arises from the plastic tube itself. Figure 4.3(d) shows the transient PA image which is the amplitude of the exponential fit over a series of PA images obtained with increasing pump-probe delay times and with both lasers on. Although the transient PA signal is smaller than even the PA signal at 830 nm, PALI imaging is able to detect it efficiently and to correctly reflect the structure of the tube.

4.3.2 *Animal imaging*

We conducted a preliminary experiment to show the application of multimodal imaging to a volume of tissue by imaging a euthanized mouse's hindlimb stained with MB. The US image shows the outline of the hindlimb of the mouse and the tip of the fiber bundle in contact with the surface of the skin (Figure 4.5(a)). This close configuration was initially chosen to maximize light delivery. The PA images obtained with pump and probe laser only show a penetration depth of 6-7 mm, however there is strong PA signal coming from outside the tissue at the location of the fiber bundle and below it (Figure 4.5(b-c)). The

transient PA image obtained from the exponential fit shows both a sparse and low intensity signal inside the tissue and a high intensity signal at the location of the fiber bundle and in the first 2 mm of tissue (Figure 4.5(d)). Furthermore, the goodness of fit was not very good leading us to choose a low R^2 threshold of 0.7. Overall, the region of tissue where we can confidently identify transient absorption is limited and the penetration depth is poor.

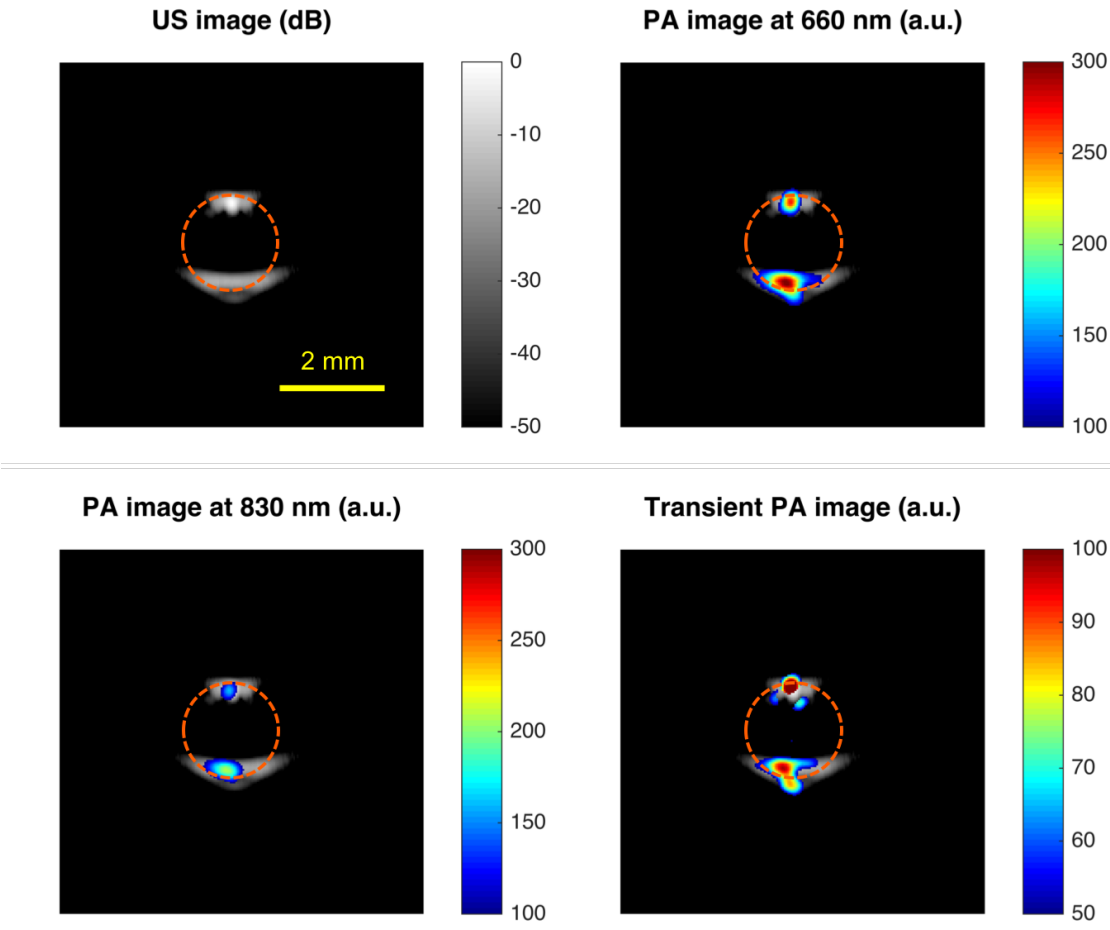

Figure 4.4. Multimodal imaging of a tube filled with MB (100 µM). (a) US image in dB scale. Dashed line shows the position of the tube. (b) PA image at 660 nm. This corresponds to the spatial absorption of light by MB molecules. (c) PA image at 830 nm. This corresponds to the background absorption by the plastic tube. (d) Transient PALI amplitude calculated from the exponential fit. Data points shown for $R^2 > 0.9$.

Finally, the oxygen partial pressure (pO_2) image was calculated by converting the photoacoustic lifetime (Figure 4.5(e)) into pO_2 using the Stern-Volmer relationship introduced in Chapter 1 (Figure 4.5(f)). The pixels in the first 1-2 mm from the surface showed a pO_2 in the 40-180 mmHg range, near the pO_2 value in air at approximately 160 mmHg [129]. From about 4 to 7 mm from the surface, the pO_2 was in the 5-120 mmHg range. pO_2 level in the femoral muscle of a live mouse was found to be 10.6 ± 1.8 mmHg at 25°C and 29.1 ± 7.8 mmHg at 37°C [130]. Then again, the low R^2 value throughout the pixels introduces a level of uncertainty in the pO_2 results, which makes the above results inconclusive.

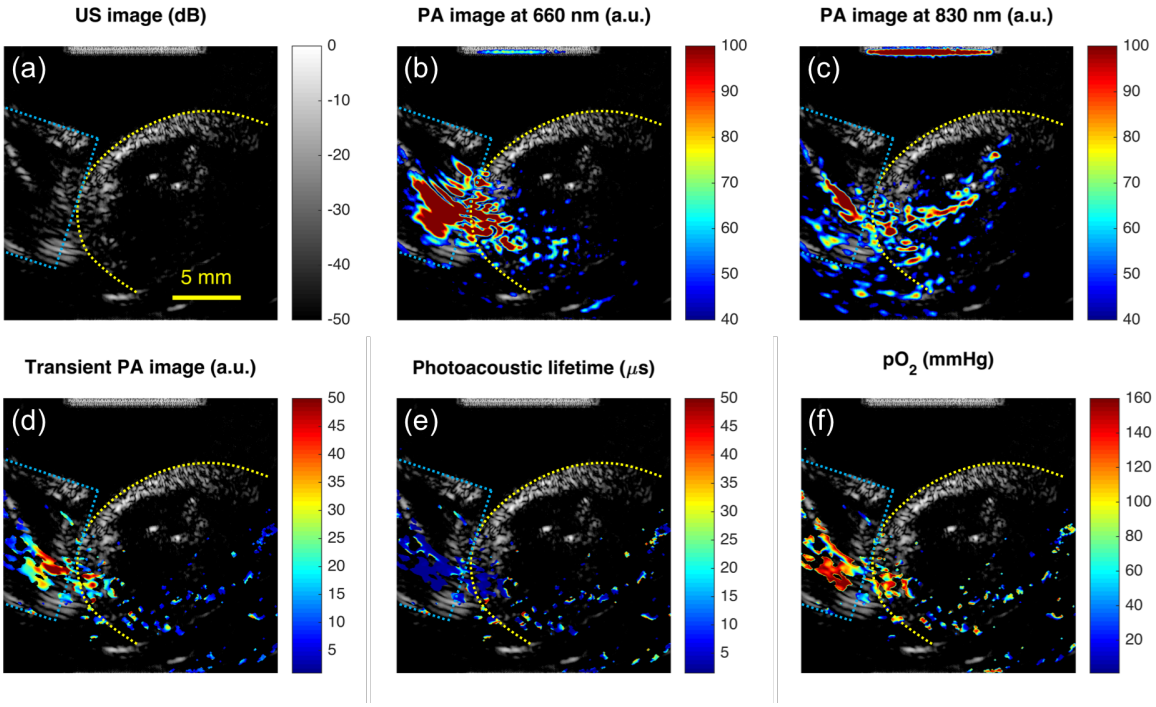

Figure 4.5. Multimodal imaging of a euthanized mouse. (a) US image of the hindlimb of a mouse in dB scale. Yellow dashed line represents the hindlimb. Blue dashed line shows the lightguide. (b) PA image at 660 nm shows the penetration depth of the pump laser pulse. (c) Background PA tissue absorption at 830 nm. (d) Transient PALI amplitude calculated from the exponential fit. Data points shown for $R^2 > 0.7$. (e) PA lifetime in μs. (f) Oxygen partial pressure (pO_2) in mmHg.

The low and heterogeneous transient photoacoustic signal may be attributed to different causes:

1. *The shadowing of acoustic energy by the fiber bundle*. In this experiment the fiber bundle was placed close to the skin surface at an 80° angle with the US transducer. In retrospect, this configuration may have caused ultrasonic reflection at the surface of the fiber bundle instead of propagation towards the US transducer. In addition, the fiber bundle generated some artifacts causing signals to appear outside the tissue, which complicates the identification of photoacoustic lifetime signal arising from MB transient absorption.

2. *Low laser energy*. At around the time of the experiment we had been dealing with a progressive loss in pump energy at the fiber output from 20-22 mJ to 12-13 mJ over the course of several weeks. Lower laser energy translates into lower power density resulting into less pump energy being absorbed by MB molecules, which can ultimately impact the photoacoustic lifetime signal amplitude.

3. *MB aggregation and lifetime quenching*. Considering a stained volume of tissue with dimensions 15x15x15 mm, the MB concentration inside the stained tissue was 2.96 x 10^{-4} M, which is comparable to the dissociation constant calculated in Chapter 2. The implication is that approximately half of the MB molecules would be dimerized at the same concentration in solution. In addition, MB is a cationic dye that can bind to the plasma membrane [131], which can result in local aggregation of MB molecules at high concentrations. We posit that at least a fraction of MB molecules are present as dimers within the stained tissue, and that this fraction does not contribute to photoacoustic lifetime signal generation due to static quenching.

4.4 PROPOSED IMPROVEMENTS AND REMAINING CHALLENGES

In future experiments, we recommend that the distance and the angle between the fiber bundle and the US transducer be investigated to yield the maximum of light delivery and acoustic propagation without obstructing the field of view. This can be accomplished by creating an adjustable holder that binds fiber and transducer together and could also ensure a repeatable positioning of these two elements across different experiments (Figure 4.6). 3d printing can be used to design and produce a prototype for this holder. In the design described in this section, the current circular fiber bundle has been replaced by a fiber bundle bifurcated on both sides with two rectangular output terminals (Figure 4.6(a)). The individual fibers in the input section are randomized in the middle section and then split to deliver a homogenized beam containing both pump and probe beams. This allows for a more uniform and symmetrical illumination of the target object or tissue. Because the fibers are split between the two terminals, the output energy is also divided by half in both bundles. Therefore, the maximum of laser energy deposition occurs where the output beams overlap (Figure 4.6(b)). Alternatively, a focusing length system at the tip of the fiber terminals may be employed to limit the spread of the output beams. The holder prototype can be designed to allow for rotational and translational degrees of freedom to optimize the distance and the angle between the US transducer and the fiber bundle. Once an optimal position has been found, the configuration of the holder may be locked in place or a new holder may be manufactured with the chosen specifications.

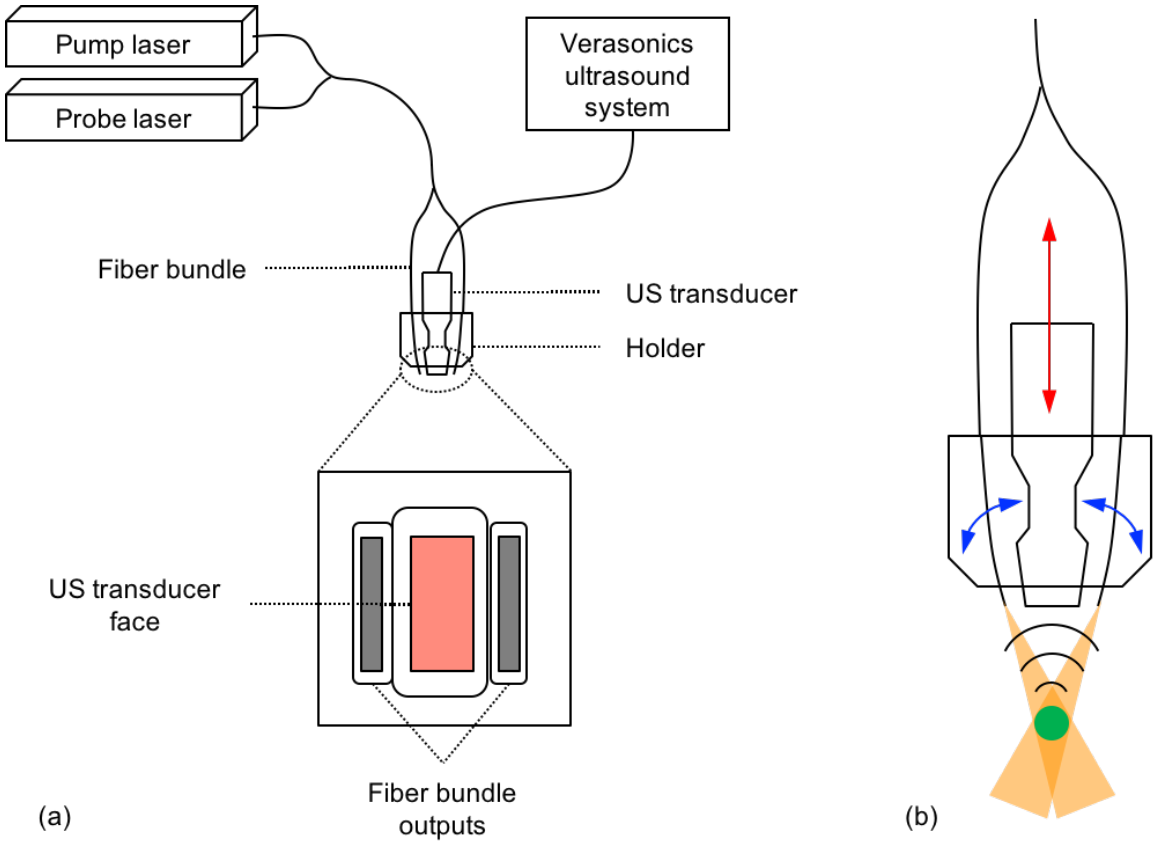

Figure 4.6. (a) Proposed design of the holder for the US transducer and fiber bundle. (b) Translational movement of the transducer and rotational movement of the fiber bundle outputs enable optimization of the distance and angle between the two.

Another area of improvement concerns laser energy normalization. Pulse-by-pulse energy variations can be effectively eliminated by performing signal averaging for each acquisition of a pump-probe delayed signal. However, slow energy drifts exist that can translate into fluence variations between acquisitions. Each laser system can be supplemented with a power/energy meter (Pulsar, Ophir Optronics) that can measure individual pulse energy. When running a MATLAB script, the pulse-by-pulse energy can be recorded in real-time, averaged for each pump-probe delay time, and the RF data can be corrected for energy variations between acquisitions. Furthermore, continuous monitoring

of laser energy may inform users if the energy decreases dramatically and if troubleshooting is necessary.

Another challenge in PALI imaging is that the excited-state lifetime of MB in *in vivo* settings can be influenced by other factors than oxygen level, such as temperature, pH, and even aggregation on biological structures such as the cell membrane. Another complex factor is depth. Indeed, the PA signal p_0 generated at any given point in space is a function of the local optical fluence Φ, which is the local optical energy per unit area [41]:

$$p_0 = \Gamma \times \mu_a \times \phi$$

where Γ is the Grüneisen parameter (a thermodynamic property of tissues) and μ_a is the local optical absorption coefficient. If the fluence was uniform throughout the imaged volume of tissue, then the PA signal would be directly proportional to the optical absorption coefficient. In practice, however, the light is attenuated as it travels through the tissue. This creates a non-linear dependence of the transient photoacoustic signal and observed excited-state lifetime with depth (Figure 4.6). The effect of pump and probe light attenuation in tissue is complex and depends on the concentration and spatial distribution of photoabsorbers – both endogenous and dye. However, the potential implications of this effect are profound at high imaging depths and would benefit from careful experimental investigation to determine the extent of the discrepancy between real and observed lifetime. Anatomically-accurate modeling of light propagation in biological tissue using the Monte-Carlo approach would also allow for a quantitative analysis of this phenomenon and may

lead to the development of a depth-dependent correction algorithm for the measured transient photoacoustic signal that could potentially increase imaging depth.

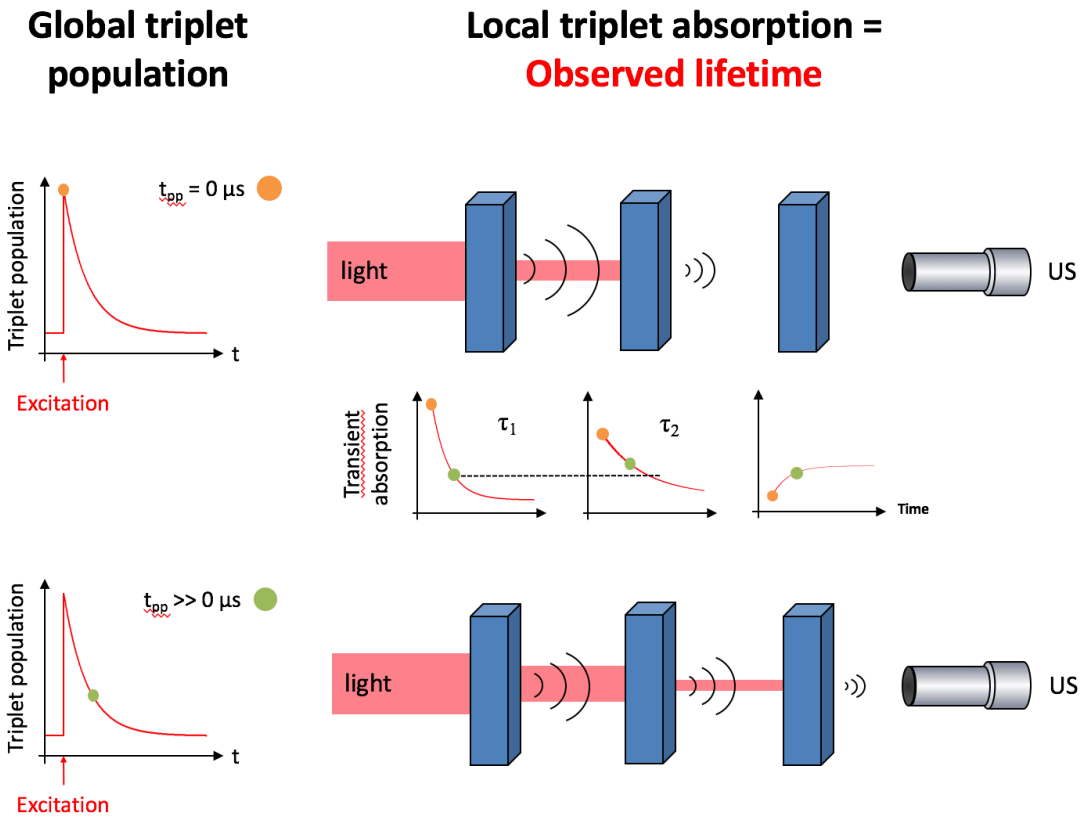

Figure 4.7. Illustration of the difference between real and measured excited-state lifetime. Fluence attenuation is manifested as decreasing light beam when travelling through layers of stained tissue. When the probing pulse is fired shortly after excitation (t_{pp} = 0 µs), the triplet population within the volume is high resulting in strong light absorption in the first layers and fast fluence attenuation. Thus, the observed transient photoacoustic signal decreases with depth. For a probing pulse fired a longer time after excitation (t_{pp} >> 0 µs), the triplet pollution has decreased due to relaxation, resulting in less absorption at the surface and slower fluence attenuation. The observed transient photoacoustic signal is then higher than for the first measurement. Consequently, exponential fitting would result in a higher and higher lifetime at increasing depths, and may even flip in regions where the light does not reach when probing close to the excitation.

Chapter 5. Summary and future directions

We have demonstrated that photoacoustic lifetime imaging (PALI) can probe the excited-state lifetime contrast between methylene blue (MB) monomers and dimers. MB monomers exhibit a long excited-state lifetime (1.8 to 79.5 μs) which decreases by three orders of magnitude upon aggregation due to static quenching. The addition of increasing concentrations of sodium sulfate, a dimerization-inducing compound, to a MB solution led to a linear decrease of the photoacoustic lifetime signal with the monomer concentration. Similarly, the addition of 4 mM sodium docecyl sulfate (SDS) – a concentration that amplifies MB aggregation and reduces the monomer concentration by more than 20-fold – led to a photoacoustic signal decrease of more than 20 dB.

We have implemented the monomer-dimer contrast mechanism for the development of an activatable photoacoustic probe for enzyme activity detection. The probe was composed of two MB chromophores conjugated to an electrostatic zipper via a flexible amino acid linker, and connected to a MMP-2 specific recognition sequence PLGLAG. In its intact state, the probe structure promotes MB dimerization and static quenching rendering low PALI signal. Enzymatic cleavage of the probe leads to the separation of MB monomers and high PALI signal. A series of activatable probes with varying zipper lengths and flexible linkers were assessed to compare their dimerization and separation efficiency, activation rate, and photoacoustic lifetime signal strength as compared to a positive and a negative control. Dimerization was highest in probes free of a flexible linker. A decrease in the initial activation rate was observed for probes with longer electrostatic zippers and probes containing a flexible linker.

Finally, we have been developing a portable multimodal system combining US/PA/PALI imaging for preclinical/clinical use. Image acquisition was programmed using an event-driven script in MATLAB. We demonstrated the capability of this system to resolve a phantom tubing object filled with MB and presented some preliminary *in vivo* results by imaging MB-stained muscle tissue in a mouse. Several improvements ideas are proposed to improve image quality and penetration depth, such as the development of a holder combining fiber bundle and ultrasound transducer into one element.

These combined results demonstrate the potential of using the new multimodal imaging system and the activatable photoacoustic probe to selectively detect enzymatic activity in a variety of physiological and disease states. The next stage is preclinical testing to evaluate the capability of the imaging system to resolve enzyme activity in vivo. Mice can be used as a cancer model for this study. Tumors with different MMP-2 expression levels will be grown in the hindlimb of a set of mice. Different modes of activatable probe administration will be investigated (e.g. tail vein or intratumorally). The mice will then be immersed in a temperature-controlled water tank and imaged by the PALI system. Blood samples will be withdrawn at regular intervals to determine probe clearance. After mice euthanasia, the tumors will be excised and the imaging results compared to tissue analysis of enzyme activity (zymography) using statistical analysis.

BIBLIOGRAPHY

[1] R. Paulmurugan, Introduction to Cancer Biology, 2012.

[2] D. Hanahan, R.A. Weinberg, Hallmarks of cancer: the next generation, Cell 144(5) (2011) 646-74.

[3] L. Migliore, F. Coppede, Genetic and environmental factors in cancer and neurodegenerative diseases, Mutat Res 512(2-3) (2002) 135-53.

[4] D.A. Camara, L.I. Mambelli, A.S. Porcacchia, I. Kerkis, Advances and Challenges on Cancer Cells Reprogramming Using Induced Pluripotent Stem Cells Technologies, J Cancer 7(15) (2016) 2296-2303.

[5] M. Verma, Personalized medicine and cancer, J Pers Med 2(1) (2012) 1-14.

[6] S. Selley, J. Donovan, A. Faulkner, J. Coast, D. Gillatt, Diagnosis, management and screening of early localised prostate cancer, Health Technol Assess 1(2) (1997) i, 1-96.

[7] T.F. Imperiale, D.F. Ransohoff, S.H. Itzkowitz, Multitarget stool DNA testing for colorectal-cancer screening, N Engl J Med 371(2) (2014) 187-8.

[8] N. Coburn, R. Przybysz, L. Barbera, D. Hodgson, S. Sharir, A. Laupacis, C. Law, CT, MRI and ultrasound scanning rates: evaluation of cancer diagnosis, staging and surveillance in Ontario, J Surg Oncol 98(7) (2008) 490-9.

[9] N.C. Institute, SEER Training: Cancer Diagnosis. https://training.seer.cancer.gov/disease/diagnosis/, (accessed March 12th.2017).

[10] P. Thampanitchawong, T. Piratvisuth, Liver biopsy:complications and risk factors, World J Gastroenterol 5(4) (1999) 301-304.

[11] A.L. Klibanov, Microbubble contrast agents: targeted ultrasound imaging and ultrasound-assisted drug-delivery applications, Invest Radiol 41(3) (2006) 354-62.

[12] N. Nitin, L.E. LaConte, O. Zurkiya, X. Hu, G. Bao, Functionalization and peptide-based delivery of magnetic nanoparticles as an intracellular MRI contrast agent, J Biol Inorg Chem 9(6) (2004) 706-12.

[13] J.R. de Boer, J. Pruim, B.F. van der Laan, T.H. Que, A.T. Willemsen, F.W. Albers, W. Vaalburg, L-1-11C-tyrosine PET in patients with laryngeal carcinomas: comparison of standardized uptake value and protein synthesis rate, J Nucl Med 44(3) (2003) 341-6.

[14] C.-H. Tung, Fluorescent peptide probes for in vivo diagnostic imaging, Peptide Science 76(5) (2004) 391-403.

[15] S. Bloch, F. Lesage, L. McIntosh, A. Gandjbakhche, K. Liang, S. Achilefu, Whole-body fluorescence lifetime imaging of a tumor-targeted near-infrared molecular probe in mice, Journal of Biomedical Optics 10(5) (2005) 054003.

[16] T. Jiang, E.S. Olson, Q.T. Nguyen, M. Roy, P.A. Jennings, R.Y. Tsien, Tumor imaging by means of proteolytic activation of cell-penetrating peptides, Proc Natl Acad Sci U S A 101(51) (2004) 17867-72.

[17] S. Henkenjohann, M. Sauer, Photoinduced electron transfer probes for the observation of enzyme activities, SPIE Proceedings 718503 (2009).

[18] J.O. McIntyre, R.L. Scherer, L.M. Matrisian, Near-infrared optical proteolytic beacons for in vivo imaging of matrix metalloproteinase activity, Methods in Molecular Biology 622 (2010) 279-304.

[19] J.H. Ryu, A. Lee, J.H. Na, S. Lee, H.J. Ahn, J.W. Park, C.-H. Ahn, B.-S. Kim, I.C. Kwon, K. Choi, I. Youn, K. Kim, Optimization of matrix metalloproteinase fluorogenic probes for osteoarthritis imaging, Amino Acids 41(5) (2011) 1113-1122.

[20] C.R. Drake, D.C. Miller, E.F. Jones, Activatable optical probes for the detection of enzymes, Current Organic Synthesis 8(4) (2011) 498-520.

[21] V. Ntziachristos, C.-H. Tung, C. Bremer, R. Weissleder, Fluorescence molecular tomography resolves protease activity *in vivo*, Nature Medicine 8 (2002) 757 - 761.

[22] K.S. Valluru, J.K. Willmann, Clinical photoacoustic imaging of cancer, Ultrasonography 35(4) (2016) 267-80.

[23] A. Dragulescu-Andrasi, S.R. Kothapalli, G.A. Tikhomirov, J. Rao, S.S. Gambhir, Activatable oligomerizable imaging agents for photoacoustic imaging of furin-like activity in living subjects, J Am Chem Soc 135(30) (2013) 11015-22.

[24] J.A. Joyce, J.W. Pollard, Microenvironmental regulation of metastasis, Nat Rev Cancer 9(4) (2009) 239-52.

[25] S.D. Mason, J.A. Joyce, Proteolytic networks in cancer, Trends Cell Biol 21(4) (2011) 228-37.

[26] B.W. Ennis, L.M. Matrisian, Matrix degrading metalloproteinases, J Neurooncol 18(2) (1994) 105-9.

[27] C. Gialeli, A.D. Theocharis, N.K. Karamanos, Roles of matrix metalloproteinases in cancer progression and their pharmacological targeting, Febs j 278(1) (2011) 16-27.

[28] M. Stearns, M.E. Stearns, Evidence for increased activated metalloproteinase 2 (MMP-2a) expression associated with human prostate cancer progression, Oncol Res 8(2) (1996) 69-75.

[29] D. Trudel, Y. Fradet, F. Meyer, F. Harel, B. Tetu, Significance of MMP-2 expression in prostate cancer: an immunohistochemical study, Cancer Res 63(23) (2003) 8511-5.

[30] A. Babusyte, K. Stravinskaite, J. Jeroch, J. Lotvall, R. Sakalauskas, B. Sitkauskiene, Patterns of airway inflammation and MMP-12 expression in smokers and ex-smokers with COPD, Respir Res 8 (2007) 81.

[31] C.M. Lee, D. Jang, S.J. Cheong, M.H. Jeong, E.M. Kim, D.W. Kim, S.T. Lim, M.H. Sohn, H.J. Jeong, Optical imaging of MMP expression and cancer progression in an inflammation-induced colon cancer model, Int J Cancer 131(8) (2012) 1846-53.

[32] T. Sorsa, P. Mantyla, T. Tervahartiala, P.J. Pussinen, J. Gamonal, M. Hernandez, MMP activation in diagnostics of periodontitis and systemic inflammation, J Clin Periodontol 38(9) (2011) 817-9.

[33] K.S. Kim, H.M. Choi, Y.A. Lee, I.A. Choi, S.H. Lee, S.J. Hong, H.I. Yang, M.C. Yoo, Expression levels and association of gelatinases MMP-2 and MMP-9 and collagenases MMP-1 and MMP-13 with VEGF in synovial fluid of patients with arthritis, Rheumatol Int 31(4) (2011) 543-7.

[34] W.T. Chia, Y.W. Chen, L.Y. Cheng, H.S. Lee, D.M. Chang, H.K. Sytwu, MMP-9 mRNA as a therapeutic marker in acute and chronic stages of arthritis induced by type II collagen antibody, J Formos Med Assoc 107(3) (2008) 245-52.

[35] P. Pradhan-Palikhe, P. Vikatmaa, T. Lajunen, A. Palikhe, M. Lepantalo, T. Tervahartiala, T. Salo, P. Saikku, M. Leinonen, P.J. Pussinen, T. Sorsa, Elevated MMP-8 and decreased myeloperoxidase concentrations associate significantly with the risk for peripheral atherosclerosis disease and abdominal aortic aneurysm, Scand J Immunol 72(2) (2010) 150-7.

[36] S.M. Clee, A role for MMP-3 genetic variation in atherosclerosis susceptibility?, Atherosclerosis 208(1) (2010) 30-1.

[37] E.I. Deryugina, J.P. Quigley, Matrix metalloproteinases and tumor metastasis, Cancer Metastasis Review 25(1) (2006) 9-34.

[38] C.M. Overall, O. Kleifeld, Validating matrix metalloproteinases as drug targets and anti-targets for cancer therapy, Nat Rev Cancer 6(3) (2006) 227-39.

[39] S. Ashkenazi, Photoacoustic lifetime imaging of dissolved oxygen using methylene blue, J Biomed Opt 15(4) (2010) 040501.

[40] C.G. Sauer, A. Kappeler, M. Spath, J.J. Kaden, M.S. Michel, D. Mayer, U. Bleyl, R. Grobholz, Expression and activity of matrix metalloproteinases-2 and -9 in serum, core needle biopsies and tissue specimens of prostate cancer patients, Virchows Arch 444(6) (2004) 518-26.

[41] Y. Zhang, H. Hong, W. Cai, Photoacoustic imaging, Cold Spring Harbor Protocols (2011) 1015-1025.

[42] K.H. Song, L.V. Wang, Deep reflection-mode photoacoustic imaging of biological tissue, J Biomed Opt 12(6) (2007) 060503.

[43] L.V. Wang, Prospects of photoacoustic tomography, Med Phys 35(12) (2008) 5758-67.

[44] G. Kim, S.W. Huang, K.C. Day, M. O'Donnell, R.R. Agayan, M.A. Day, R. Kopelman, S. Ashkenazi, Indocyanine-green-embedded PEBBLEs as a contrast agent for photoacoustic imaging, J Biomed Opt 12(4) (2007) 044020.

[45] A. Agarwal, S.W. Huang, M. O'Donnell, K.C. Day, M. Day, N. Kotov, S. Ashkenazi, Targeted gold nanorod contrast agent for prostate cancer detection by photoacoustic imaging, Journal of Applied Physics 102(6) (2007) 064701-064701-4.

[46] A. De la Zerda, C. Zavaleta, S. Keren, S. Vaithilingam, S. Bodapati, Z. Liu, J. Levi, B.R. Smith, T.J. Ma, O. Oralkan, Z. Cheng, X. Chen, H. Dai, B.T. Khuri-Yakub, S.S. Gambhir, Carbon nanotubes as photoacoustic molecular imaging agents in living mice, Nat Nanotechnol, England, 2008, pp. 557-62.

[47] E.V. Shashkov, M. Everts, E.I. Galanzha, V.P. Zharov, Quantum dots as multimodal photoacoustic and photothermal contrast agents, Nano Lett 8(11) (2008) 3953-8.

[48] Y. Lao, D. Xing, S. Yang, L. Xiang, Noninvasive photoacoustic imaging of the developing vasculature during early tumor growth, Phys Med Biol 53(15) (2008) 4203-12.

[49] L. Song, C. Kim, K. Maslov, K.K. Shung, L.V. Wang, High-speed dynamic 3D photoacoustic imaging of sentinel lymph node in a murine model using an ultrasound array, Med Phys 36(8) (2009) 3724-9.

[50] J.T. Oh, M.L. Li, H.F. Zhang, K. Maslov, G. Stoica, L.V. Wang, Three-dimensional imaging of skin melanoma in vivo by dual-wavelength photoacoustic microscopy, J Biomed Opt 11(3) (2006) 34032.

[51] M. Gonzalez-Bejar, P. Montes-Navajas, H. Garcia, J.C. Scaiano, Methylene blue encapsulation in cucurbit[7]uril: laser flash photolysis and near-IR luminescence studies of the interaction with oxygen, Langmuir 25(18) (2009) 10490-4.

[52] Q. Shao, E. Morgounova, C. Jiang, J. Choi, J. Bischof, S. Ashkenazi, In vivo photoacoustic lifetime imaging of tumor hypoxia in small animals, Journal of biomedical optics 18(7) (2013) 076019-076019.

[53] M.H. Pedersen, K.L. Gammelmark, J.A. Jensen, In-vivo evaluation of convex array synthetic aperture imaging, Ultrasound Med Biol 33(1) (2007) 37-47.

[54] D. Razansky, N.J. Harlaar, J.L. Hillebrands, A. Taruttis, E. Herzog, C.J. Zeebregts, G.M. van Dam, V. Ntziachristos, Multispectral optoacoustic tomography of matrix metalloproteinase activity in vulnerable human carotid plaques, Mol Imaging Biol 14(3) (2012) 277-85.

[55] J. Levi, S.R. Kothapalli, T.J. Ma, K. Hartman, B.T. Khuri-Yakub, S.S. Gambhir, Design, synthesis, and imaging of an activatable photoacoustic probe, J Am Chem Soc 132(32) (2010) 11264-9.

[56] A.H. Green, J.R. Norris, J. Wang, Z. Xie, H.F. Zhang, P.J. La Riviere, In vitro testing of a protease-sensitive contrast agent for optoacoustic imaging, Journal of Biomedical Optics 15(2) (2010).

[57] J. Xiao, Z. Yuan, J. He, H. Jiang, Quantitative multispectral photoacoustic tomography and wavelength optimization, J Xray Sci Technol 18(4) (2010) 415-27.

[58] B.T. Cox, J.G. Laufer, P.C. Beard, The challenges for quantitative photoacoustic imaging, SPIE Photonics West, Proc. of SPIE, San Francisco, 2009, pp. 717713-1 - 717713-9.

[59] K.J. Willis, A.G. Szabo, M. Zuker, J.M. Ridgeway, B. Alpert, Fluorescence decay kinetics of the tryptophyl residues of myoglobin: effect of heme ligation and evidence for discrete lifetime components, Biochemistry 29(22) (1990) 5270-5.

[60] E. Dimitrow, I. Riemann, A. Ehlers, M.J. Koehler, J. Norgauer, P. Elsner, K. Konig, M. Kaatz, Spectral fluorescence lifetime detection and selective melanin imaging by multiphoton laser tomography for melanoma diagnosis, Exp Dermatol 18(6) (2009) 509-15.

[61] A. van Hoek, J. Vervoort, A.J. Visser, A subnanosecond resolving spectrofluorimeter for the analysis of protein fluorescence kinetics, J Biochem Biophys Methods 7(3) (1983) 243-54.

[62] J.M. Beechem, L. Brand, Time-resolved fluorescence of proteins, Annu Rev Biochem 54(1) (1985) 43-71.

[63] H.C. Junqueira, D. Severino, L.G. Dias, M.S. Gugliotti, M.S. Baptista, Modulation of methylene blue photochemical properties based on adsorption at aqueous micelle interfaces, Phys. Chem. Chem. Phys. 4 (2002) 2320-2328.

[64] I.F. Tannock, D. Rotin, Acid pH in tumors and its potential for therapeutic exploitation, Cancer Res 49(16) (1989) 4373-84.

[65] E. Rabinowitch, L.F. Epstein, Polymerization of Dyestuffs in Solution. Thionine and Methylene Blue, J. Am. Chem. Soc. 63(1) (1941) 69–78.

[66] J. Chen, T.C. Cesario, P.M. Rentzepis, Effect of pH on methylene blue transient states and kinetics and bacteria photoinactivation, Journal of Physical Chemistry A 115(13) (2011) 2702-2707.

[67] P.-C. Li, C.-R.C. Wang, D.-B. Shieh, C.-W. Wei, C.-K. Liao, C. Poe, S. Jhan, A.-A. Ding, Y.-N. Wu, In vivo photoacoustic molecular imaging with simultaneous multiple selective targeting using antibody-conjugated gold nanorods, Optics Express 16(23) (2008) 18605-18615.

[68] R.W. Redmond, J.N. Gamlin, A compilation of singlet oxygen yields from biologically relevant molecules, Photochemistry and Photobiology 70(4) (1999) 391–475.

[69] D. Severino, H.C. Junqueira, M. Gugliotti, D.S. Gabrielli, M.S. Baptista, Influence of negatively charged interfaces on the ground and excited state properties of methylene blue, Photochemistry and Photobiology 77(5) (2003) 459-468.

[70] S. Tyagi, F.R. Kramer, Molecular beacons: Probes that fluoresce upon hybridization, Nature Biotechnology 14(3) (1996) 303-308.

[71] A. Garcia-Uribe, J. Zou, M. Duvic, J.H. Cho-Vega, V.G. Prieto, L.V. Wang, In vivo diagnosis of melanoma and nonmelanoma skin cancer using oblique incidence diffuse reflectance spectrometry, Cancer Research 72(11) (2012) 2738-2745.

[72] M. Heijblom, D. Piras, W. Xia, J.C. van Hespen, J.M. Klaase, F.M. van den Engh, T.G. van Leeuwen, W. Steenbergen, S. Manohar, Visualizing breast cancer using the Twente photoacoustic mammoscope: what do we learn from twelve new patient measurements?, Optics Express 20(11) (2012) 11582-11597.

[73] J.I. Clifton, J.B. Leikin, Methylene Blue, American Journal of Therapeutics 10(4) (2003) 289-291.

[74] K. Orth, G. Beck, F. Genze, A. Rück, Methylene blue mediated photodynamic therapy in experimental colorectal tumors in mice, Journal of Photochemistry and Photobiology B: Biology 57(2-3) (2000) 186-192.

[75] A.R. DiSanto, J.G. Wagner, Pharmacokinetics of highly ionized drugs. II. Methylene blue--absorption, metabolism, and excretion in man and dog after oral administration, J Pharm Sci 61(7) (1972) 1086-90.

[76] C. Peter, D. Hongwan, A. Kupfer, B.H. Lauterburg, Pharmacokinetics and organ distribution of intravenous and oral methylene blue, Eur J Clin Pharmacol 56(3) (2000) 247-50.

[77] O. Yazdani, M. Irandoust, J.B. Ghasemi, S.H. Hooshmand, Thermodynamic study of the dimerization equilibrium of methylene blue, methylene green and thiazole orange at various surfactant concentrations and different ionic strengths and in mixed solvents by spectral titration and chemometric analysis, Dyes and Pigments 92(3) (2012) 1031-1041.

[78] K. Patil, R. Pawar, P. Talap, Self-aggregation of Methylene Blue in aqueous medium and aqueous solutions of Bu_4NBr and urea, Phys. Chem. Chem. Phys. 2 (2000) 4313-4317.

[79] T. Förster, Energy migration and fluorescence, Journal of Biomedical Optics 17(1) (2012) 011002.

[80] M. Kasha, Energy Transfer Mechanisms and the Molecular Exciton Model for Molecular Aggregates, Radiation Research 20(1) (1963) 55-71.

[81] M. Kasha, H.R. Rawls, M. Ashraf El-Bayoumi, The exciton model in molecular spectroscopy, *Pure and Applied Chemistry* 11(3-4) (1965) 371-392.

[82] A. Weller, Electron-transfer and complex formation in the excited state, Pure Applied Chemistry 16 (1968) 115.

[83] S. Doose, H. Neuweiler, M. Sauer, Fluorescence quenching by photoinduced electron transfer: a reporter for conformational dynamics of macromolecules, ChemPhysChem 10(9-10) (2009) 1389-1398.

[84] R.M. Danziger, K.H. Bar-Eli, K. Weiss, The laser photolysis of methylene blue, J. Phys. Chem. 71(8) (1967) 2633-2640.

[85] R.S. Sonawane, S.G. Hegde, M.K. Dongare, Preparation of titanium(IV) oxide thin film photocatalyst by sol–gel dip coating, Materials Chemistry and Physics 77(3) (2003) 744–750.

[86] J. Cenens, R.A. Schoonheydt, Visible spectroscopy of methylene blue on hectorite, laponite B and barasym in aqueous suspension, Clays and Clay Minerals 36(3) (1988) 214-224.

[87] E. Touitou, P. Fisher, Prevention of molecular self-association by sodium salicylate: Effect on methylene blue, Journal of Pharmaceutical Sciences 75(4) (1986) 384-386.

[88] M.K. Carroll, M.A. Unger, A.M. Leach, M.J. Morris, C.M. Ingersoll, F.V. Bright, Interactions between methylene blue and sodium dodecyl sulfate in aqueous solution studied by molecular spectroscopy, Applied spectroscopy 53(7) (1999) 780-784.

[89] X. Liu, X. Wu, J. Yang, Protein determination using methylene blue in a synchronous fluorescence technique, Talanta 81(3) (2010) 760-765.

[90] J. Zhang, Y. Ma, S.S. Taylor, R.Y. Tsien, Genetically encoded reporters of protein kinase A activity reveal impact of substrate tethering, Proc Natl Acad Sci U S A 98(26) (2001) 14997-5002.

[91] S. Liu, J. Zhang, Y.K. Xiang, FRET-based direct detection of dynamic protein kinase A activity on the sarcoplasmic reticulum in cardiomyocytes, Biochem Biophys Res Commun 404(2) (2011) 581-6.

[92] V.V. Didenko, DNA probes using fluorescence resonance energy transfer (FRET): designs and applications, Biotechniques 31(5) (2001) 1106-16, 1118, 1120-1.

[93] R. Weissleder, C.-H. Tung, U. Mahmood, A.J. Bogdanov, In vivo imaging of tumors with protease-activated near-infrared fluorescent probes, Nature Biotechnology 17(4) (1999) 375-378.

[94] J. Levi, S.R. Kothapalli, S. Bohndiek, J.K. Yoon, A. Dragulescu-Andrasi, C. Nielsen, A. Tisma, S. Bodapati, G. Gowrishankar, X. Yan, C. Chan, D. Starcevic, S.S. Gambhir, Molecular photoacoustic imaging of follicular thyroid carcinoma, Clin Cancer Res 19(6) (2013) 1494-502.

[95] L.V. Wang, S. Hu, Photoacoustic tomography: in vivo imaging from organelles to organs, Science 335(6075) (2012) 1458-62.

[96] Y. Liu, L. Nie, X. Chen, Photoacoustic Molecular Imaging: From Multiscale Biomedical Applications Towards Early-Stage Theranostics, Trends Biotechnol 34(5) (2016) 420-33.

[97] J. Weber, P.C. Beard, S.E. Bohndiek, Contrast agents for molecular photoacoustic imaging, Nat Methods 13(8) (2016) 639-50.

[98] L. Nie, X. Chen, Structural and functional photoacoustic molecular tomography aided by emerging contrast agents, Chem Soc Rev 43(20) (2014) 7132-70.

[99] A.K. Iyer, G. Khaled, J. Fang, H. Maeda, Exploiting the enhanced permeability and retention effect for tumor targeting, Drug Discov Today 11(17-18) (2006) 812-8.

[100] Q. Miao, K. Pu, Emerging Designs of Activatable Photoacoustic Probes for Molecular Imaging, Bioconjug Chem 27(12) (2016) 2808-2823.

[101] K. Yang, L. Zhu, L. Nie, X. Sun, L. Cheng, C. Wu, G. Niu, X. Chen, Z. Liu, Visualization of protease activity in vivo using an activatable photo-acoustic imaging probe based on CuS nanoparticles, Theranostics 4(2) (2014) 134.

[102] H. Li, P. Zhang, L.P. Smaga, R.A. Hoffman, J. Chan, Photoacoustic Probes for Ratiometric Imaging of Copper(II), J Am Chem Soc 137(50) (2015) 15628-31.

[103] K. Pu, A.J. Shuhendler, J.V. Jokerst, J. Mei, S.S. Gambhir, Z. Bao, J. Rao, Semiconducting polymer nanoparticles as photoacoustic molecular imaging probes in living mice, Nature nanotechnology 9(3) (2014) 233-239.

[104] Q.Q. Miao, Y. Lyu, D. Ding, K.Y. Pu, Semiconducting Oligomer Nanoparticles as an Activatable Photoacoustic Probe with Amplified Brightness for In Vivo Imaging of pH, Advanced Materials 28(19) (2016) 3662-3668.

[105] J. Song, J. Kim, S. Hwang, M. Jeon, S. Jeong, C. Kim, S. Kim, "Smart" gold nanoparticles for photoacoustic imaging: an imaging contrast agent responsive to the cancer microenvironment and signal amplification via pH-induced aggregation, Chem Commun (Camb) 52(53) (2016) 8287-90.

[106] K.K. Ng, M. Shakiba, E. Huynh, R.A. Weersink, A. Roxin, B.C. Wilson, G. Zheng, Stimuli-responsive photoacoustic nanoswitch for in vivo sensing applications, ACS Nano 8(8) (2014) 8363-73.

[107] D. Razansky, N.J. Harlaar, J.L. Hillebrands, A. Taruttis, E. Herzog, C.J. Zeebregts, G.M. van Dam, V. Ntziachristos, Multispectral optoacoustic tomography of matrix metalloproteinase activity in vulnerable human carotid plaques, Molecular imaging and biology 14(3) (2012) 277-285.

[108] K. Jansen, G. van Soest, A.F. van der Steen, Intravascular photoacoustic imaging: a new tool for vulnerable plaque identification, Ultrasound Med Biol 40(6) (2014) 1037-48.

[109] K. Yang, L. Zhu, L. Nie, X. Sun, L. Cheng, C. Wu, G. Niu, X. Chen, Z. Liu, Visualization of protease activity in vivo using an activatable photo-acoustic imaging probe based on CuS nanoparticles, Theranostics 4(2) (2014) 134-41.

[110] K. Pu, A.J. Shuhendler, J.V. Jokerst, J. Mei, S.S. Gambhir, Z. Bao, J. Rao, Semiconducting polymer nanoparticles as photoacoustic molecular imaging probes in living mice, Nat Nanotechnol 9(3) (2014) 233-9.

[111] A. Forbrich, P. Shao, W. Shi, R.J. Zemp, Lifetime-weighted photoacoustic imaging, SPIE BiOS, International Society for Optics and Photonics, 2015, pp. 93231H-93231H-6.

[112] A.E. O'Connor, W.M. Gallagher, A.T. Byrne, Porphyrin and nonporphyrin photosensitizers in oncology: preclinical and clinical advances in photodynamic therapy, Photochem Photobiol 85(5) (2009) 1053-74.

[113] R. Weissleder, A clearer vision for in vivo imaging, Nat Biotechnol, United States, 2001, pp. 316-7.

[114] E. Morgounova, Q. Shao, B.J. Hackel, D.D. Thomas, S. Ashkenazi, Photoacoustic lifetime contrast between methylene blue monomers and self-quenched dimers as a model for dual-labeled activatable probes, J Biomed Opt 18(5) (2013) 56004.

[115] S.M. van Duijnhoven, M.S. Robillard, K. Nicolay, H. Grull, Tumor targeting of MMP-2/9 activatable cell-penetrating imaging probes is caused by tumor-independent activation, J Nucl Med 52(2) (2011) 279-86.

[116] M.T.M. Rood, M. Raspe, J.B. ten Hove, K. Jalink, A.H. Velders, F.W.B. van Leeuwen, MMP-2/9-Specific Activatable Lifetime Imaging Agent, Sensors 15(5) (2015) 11076-11091.

[117] B.K. Kay, M.P. Williamson, P. Sudol, The importance of being proline: the interaction of proline-rich motifs in signaling proteins with their cognate domains, Faseb Journal 14(2) (2000) 231-241.

[118] K. Kessenbrock, V. Plaks, Z. Werb, Matrix metalloproteinases: regulators of the tumor microenvironment, Cell 141(1) (2010) 52-67.

[119] R.P. Iyer, N.L. Patterson, G.B. Fields, M.L. Lindsey, The history of matrix metalloproteinases: milestones, myths, and misperceptions, Am J Physiol Heart Circ Physiol 303(8) (2012) H919-30.

[120] L.J. McCawley, L.M. Matrisian, Matrix metalloproteinases: they're not just for matrix anymore!, Curr Opin Cell Biol 13(5) (2001) 534-40.

[121] I. Stamenkovic, Matrix metalloproteinases in tumor invasion and metastasis, Semin Cancer Biol 10(6) (2000) 415-33.

[122] M. Toth, R. Fridman, Assessment of Gelatinases (MMP-2 and MMP-9) by Gelatin Zymography, in: J.M. Walker (Ed.), Methods in Molecular Medicine. Volume 1: Analysis of Cells and Tissues, Humana Press, Totowa, New Jersey, 2001, pp. 163-174.

[123] A. Mishra, R.K. Behera, P.K. Behera, B.K. Mishra, G.B. Behera, Cyanines during the 1990s: A Review, Chem Rev 100(6) (2000) 1973-2012.

[124] A. Jonsson, C. Hjalmarsson, P. Falk, M.L. Ivarsson, Levels of matrix metalloproteinases differ in plasma and serum - aspects regarding analysis of biological markers in cancer, Br J Cancer 115(6) (2016) 703-6.

[125] H. Nagase, R. Visse, G. Murphy, Structure and function of matrix metalloproteinases and TIMPs, Cardiovasc Res 69(3) (2006) 562-73.

[126] G. Morgia, M. Falsaperla, G. Malaponte, M. Madonia, M. Indelicato, S. Travali, M.C. Mazzarino, Matrix metalloproteinases as diagnostic (MMP-13) and prognostic (MMP-2, MMP-9) markers of prostate cancer, Urol Res 33(1) (2005) 44-50.

[127] J.A. Jensen, S.I. Nikolov, K.L. Gammelmark, M.H. Pedersen, Synthetic aperture ultrasound imaging, Ultrasonics 44 Suppl 1 (2006) e5-15.

[128] I. Trots, A. Nowicki, M. Lewandowski, Synthetic Transmit Aperture in Ultrasound Imaging, Archives of Acoustics 34(4) (2009).

[129] M.C. Brahimi-Horn, J. Pouyssegur, Oxygen, a source of life and stress, FEBS Lett 581(19) (2007) 3582-91.

[130] A. Matsumoto, S. Matsumoto, A.L. Sowers, J.W. Koscielniak, N.J. Trigg, P. Kuppusamy, J.B. Mitchell, S. Subramanian, M.C. Krishna, K. Matsumoto, Absolute oxygen tension (pO(2)) in murine fatty and muscle tissue as determined by EPR, Magn Reson Med 54(6) (2005) 1530-5.

[131] T.F. Schmidt, L. Caseli, O.N. Oliveira, Jr., R. Itri, Binding of methylene blue onto Langmuir monolayers representing cell membranes may explain its efficiency as photosensitizer in photodynamic therapy, Langmuir 31(14) (2015) 4205-12.